JEM Journal of Experimental Medicine

ARTICLE

Periductal fibroblasts participate in liver homeostasis, fibrosis, and tumorigenesis

Shan-Shan Wang[1*], Jia Yuan[1*], Xinyu Thomas Tang[2,3], Xiujuan Yin[2], Ke Fang[2], Lin Veronica Chen[2,3], Zhenggang Ren[1], and Bo O. Zhou[2,3,4]

Hepatic fibroblasts comprise groups of stromal cells in the liver that are phenotypically distinct from hepatic stellate cells. However, their physiology is poorly understood. By single-cell RNA sequencing, we identified *Cd34* and *Dpt* as hepatic fibroblast–specific genes. *Cd34*-CreER labeled periportal-venous and periductal fibroblasts, but few pericentral-venous fibroblasts. *Cd34*$^+$ fibroblasts generated ∼25% of myofibroblasts in periportal fibrosis and ∼40% of cancer-associated fibroblasts (CAFs) in intrahepatic cholangiocarcinoma (ICC). Myofibroblast formation by *Cd34*$^+$ fibroblasts required *Tgfbr2*. Depletion of *Cd34*$^+$ fibroblasts increased the frequency of the ductal epithelial cells under homeostasis and accelerated the progression of ICC. *Dpt*-CreER labeled periportal- and pericentral-venous fibroblasts, but much less periductal fibroblasts. *Dpt*$^+$ cells generated ∼15% of myofibroblasts in periportal fibrosis, but few myofibroblasts in pericentral fibrosis or CAFs in ICC. Thus, an orthogonal combination of *Cd34*-CreER and *Dpt*-CreER dissected the fates of periductal, periportal-venous, and pericentral-venous fibroblasts. Both periductal and periportal-venous fibroblasts contribute to liver fibrosis. Periductal fibroblasts also contribute to ductal homeostasis and ICC progression.

Introduction

Hepatic fibroblasts represent a type of stromal cells in the liver that is distinct from the vitamin A–storing hepatic stellate cells (HSCs). They were originally identified as connective tissue cells surrounding the portal triad (bile duct, portal vein, and small artery) and observed to be characterized by long processes and usually surrounded by fibrils, including elastic fibers (Carruthers et al., 1962). Hepatic fibroblasts were first described as mesenchymal cells not related to sinusoids (Popper and Uenfriend, 1970; Schaffner et al., 1963). Later, fibroblast-like cells were also observed surrounding the central veins (second layer cells) and in the liver capsule beneath the mesothelium (submesothelial cells) (Bhunchet and Wake, 1992; Chapman and Eagles, 2007). Therefore, hepatic fibroblasts are a heterogeneous population that includes several anatomically different subpopulations. Although many markers, such as Col1a1, Col15a1, elastin, ectonucleoside triphosphate diphosphohydrolase 2, and Thy1, have been used to identify hepatic fibroblasts (Dranoff et al., 2002; Fausther et al., 2015; Iwaisako et al., 2014; Katsumata et al., 2017; Lemoinne et al., 2015; Li et al., 2007; Lua et al., 2016), their expression is not restricted to this population in the liver (Karin et al., 2016; Wells, 2014). Moreover, the expression patterns of these markers in different fibroblast subpopulations are also unclear. Thus, overall, our current knowledge about the cellular identity of different hepatic fibroblast subpopulations is limited.

Genetic lineage-tracing studies using HSC-specific Cre or CreER drivers have shown HSCs to be the major contributor to myofibroblast formation in liver fibrosis (Henderson et al., 2013; Mederacke et al., 2013; Wang et al., 2021). Although hepatic fibroblasts have been proposed as precursors of myofibroblasts during liver fibrosis, especially biliary fibrosis, their precise contribution remains controversial (Dranoff and Wells, 2010; Kisseleva, 2017; Wells, 2014). Recent studies have investigated the potential contributions of portal fibroblasts (identified according to the expression of a *Col1*-GFP reporter) to the myofibroblast pool during periductal fibrosis, as well as mapping their transcriptome (Iwaisako et al., 2014; Lua et al., 2016). A major challenge in understanding the contribution of hepatic fibroblasts to fibrosis lies in the similarity of the molecular signatures of fibroblasts, HSCs, and myofibroblasts. To date, Cre alleles able to distinguish the fate of hepatic fibroblasts from other non-parenchymal cells of the liver, especially HSCs, have not been available.

[1]Department of Hepatic Oncology, Liver Cancer Institute, Zhongshan Hospital, Fudan University and Key Laboratory of Carcinogenesis and Cancer Invasion, Ministry of Education, Shanghai, China; [2]Key Laboratory of Multi-Cell System, Shanghai Institute of Biochemistry and Cell Biology, CAS Center for Excellence in Molecular Cell Science, Chinese Academy of Sciences, Shanghai, China; [3]University of Chinese Academy of Sciences, Beijing, China; [4]State Key Laboratory of Experimental Hematology, Haihe Laboratory of Cell Ecosystem, Institute of Hematology & Blood Diseases Hospital, Chinese Academy of Medical Sciences & Peking Union Medical College, Tianjin, China.

*S.-S. Wang and J. Yuan contributed equally to this paper. Correspondence to Bo O. Zhou: bo.zhou@sibcb.ac.cn; Zhenggang Ren: ren.zhenggang@zs-hospital.sh.cn; Shan-Shan Wang: wang.shanshan1@zs-hospital.sh.cn.

Single-cell RNA sequencing (scRNA-seq) has now been widely used to identify cell (sub)populations within tissues, including the liver (Dobie et al., 2019; Krenkel et al., 2019; Wang et al., 2021; Yang et al., 2021). scRNA-seq also facilitates the characterization of cellular identity, allowing fine discrimination between cell types that have similar characteristics (Dobie et al., 2019). In this study, we aimed to identify fibroblast-specific genes that would enable the fate mapping of these cells in vivo. From scRNA-seq data, we found that *Cd34*, *Dpt*, and *Acta2* were expressed in hepatic fibroblasts, but not in the majority of other liver cell types, including HSCs. Furthermore, a combination of *Cd34*-CreER and *Dpt*-CreER discriminated between different subpopulations of hepatic fibroblasts. By quantifying and comparing the lineage outputs of *Cd34*-CreER$^+$ and *Dpt*-CreER$^+$ cells, we determined the respective contributions of periductal, periportal-venous, and pericentral-venous fibroblasts to ductal homeostasis, liver fibrosis, and tumorigenesis.

Results

scRNA-seq identified *Cd34*, *Dpt*, and *Acta2* as markers for hepatic fibroblasts

We aimed to identify markers that would allow the specific and inducible fate mapping of hepatic fibroblasts. To this end, we compared the single-cell transcriptomes of all liver cell types. We chose scRNA-seq datasets from Wang et al. (2021) that included most liver cell types except for vascular smooth muscle cells (VSMCs) and Dobie et al. (2019) that included HSCs, fibroblasts, and VSMCs (Fig. S1 A). These datasets were combined to ensure a complete representation of all liver cell types for our analyses, and all samples originated from normal liver conditions. t-Distributed stochastic neighbor embedding (t-SNE) analysis identified eight main cell clusters (Fig. 1 A). Based on the expression patterns of known cell type–specific marker genes (Fig. 1 B) and the top 100 differentially expressed genes (Fig. S1 B), we defined these cell types as HSCs (*Lrat*$^+$), fibroblasts (*Lrat*$^-$*Pdgfra*$^+$*Col1a1*^{high}), VSMCs (*Myh11*$^+$), mesothelial cells (*Msln*$^+$), endothelial cells (*Pecam1*$^+$), immune cells (*Ptprc*$^+$), hepatocytes (*Gnmt*$^+$), and cholangiocytes (*Sox9*$^+$).

Among known fibroblast markers, *Entpd2*, but not *Thy1*, showed robust and specific expression in fibroblasts (Fig. 1, C and D); *Col1a1* was highly expressed by fibroblasts and lowly expressed by HSCs (Fig. 1 E). Therefore, *Col1a1* expression is not sufficient to distinguish fibroblasts from HSCs. *Cd34* was highly expressed by fibroblasts and lowly expressed by mesothelial cells, but not by HSCs (Fig. 1 F). *Dpt* was specifically expressed by fibroblasts (Fig. 1 G). *Acta2* was highly expressed by VSMCs and moderately expressed by fibroblasts (Fig. 1 H). The mesothelial cell cluster expressed *Gpm6a*, *Wt1*, and *Msln* (Fig. 1, I–K), consistent with previous reports (Balog et al., 2020; Li et al., 2013; Lua et al., 2016). We chose *Cd34*, *Dpt*, and *Acta2* for the generation of fibroblast-specific lineage-tracing mice.

Cd34-CreER labeled periductal and periportal-venous, but not pericentral-venous, fibroblasts

We performed immunostaining to examine the protein expression patterns of CD34 in the liver of 2-mo-old wild-type mice. Confocal imaging was performed on 15-µm-thick liver sections co-stained with anti-CD31, anti-Epcam, and anti-CD34 antibodies (Fig. 2 A). Anti-CD31 staining depicted the whole vasculature of the liver, in which the portal and central veins were CD31$^+$ and relatively large, whereas sinusoids were CD31$^+$ and relatively small (Fig. 2 A). Anti-Epcam antibody stained the bile ducts and thereby distinguished portal from central zones (Fig. 2 A). Anti-CD34 staining was robustly detected around the CD31$^+$ portal veins and Epcam$^+$ bile ducts, but was not detected in cells surrounding CD31$^+$ sinusoids or CD31$^+$ central veins (Fig. 2 A). These data suggested that CD34$^+$ fibroblasts are mostly restricted to the periportal-venous and periductal regions.

In order to fate-map CD34$^+$ fibroblasts, we generated *Cd34*^{creER} knock-in mice, in which a *creER*^{T2} coding sequence was inserted into the *Cd34* genomic loci in front of the initiation codon ATG (Fig. S2 A). These mice were crossed with *Rosa26*$^{CAG\text{-}loxp\text{-}STOP\text{-}loxp\text{-}tdTomato}$ (*R26*^{tdTomato}) mice (Madisen et al., 2010) to constitutively label Cre-expressing cells and their descendants with Tomato fluorescent protein. Cre expression was induced at 6 wk of age, and the mice were analyzed at 8 wk of age. Co-staining of liver sections with anti-CD31 and anti-Epcam antibodies detected robust Tomato expression around CD31$^+$ portal veins and Epcam$^+$CD31$^-$ bile ducts, but not around CD31$^+$ central veins or CD31$^+$ sinusoids (Fig. 2 B). Confocal imaging of anti-CD34 antibody–stained liver sections confirmed the specific and efficient (~67%) recombination of *Cd34*-CreER in CD34$^+$ cells in the liver (Fig. 2 C and Fig. S2 C). Most of the Col1$^+$ and Thy-1$^+$ fibroblasts were labeled by Tomato around the portal triad (Fig. 2, D and E). In contrast, few VSMCs surrounding the arteries and portal veins expressed Tomato in the liver (Fig. 2 F, Fig. S1 C, and Fig. S2 D). On-slide staining of isolated nonparenchymal liver cells from *Cd34*^{creER};*R26*^{tdTomato} mice detected Tomato expression in a subset of Col1$^+$ cells, but not Reln$^+$ or Myh11$^+$ cells (Fig. S2, E–G). Whole-lobe tissue clearing and 3D reconstruction of the Tomato$^+$ cells from *Cd34*^{creER};*R26*^{tdTomato} liver outlined the portal venous/bile ductal network in the liver (Fig. S2 B). Thus, *Cd34*-CreER labeled periductal- and periportal-venous fibroblasts, but not pericentral-venous fibroblasts.

Besides the Tomato$^+$ fibroblasts around the portal triad, a few sparsely distributed Tomato$^+$ cells were also observed in the liver from *Cd34*^{creER};*R26*^{tdTomato} mice (Fig. 2 B). Confocal imaging showed that these sparsely distributed Tomato$^+$ cells were not Reln$^+$ HSCs (Fig. 2 G and Fig. S1 D), Gpm6a$^+$ mesothelial cells (Fig. 2 H), Hnf4a$^+$ hepatocytes (Fig. S2 H), or F4/80$^+$ Kupffer cells (Fig. 2 I). Most of these cells expressed the pan-immune cell marker CD45 (Fig. 2 J). Both intravascular and extravascular Tomato$^+$ cells were frequently detected on liver sections (Fig. 2 L). By flow cytometry, Tomato$^+$ cells represented ~21% of all CD45/Ter119$^+$ immune cells in the liver (Fig. 2 K). Consistent with this, ~25% of all hematopoietic stem cells in the bone marrow were Tomato$^+$ (Fig. S2 I). Flow cytometric analysis of enzymatically dissociated liver cells from *Cd34*^{creER};*R26*^{tdTomato} mice showed that Tomato expression was not detected in VE-cadherin$^+$ endothelial cells (Fig. 2 M).

Cd34-CreER–labeled fibroblasts contribute to myofibroblast and CAF formation

We then investigated the potential contribution of *Cd34*$^+$ cells to liver fibrosis. Pericentral fibrosis was induced in 2-mo-old

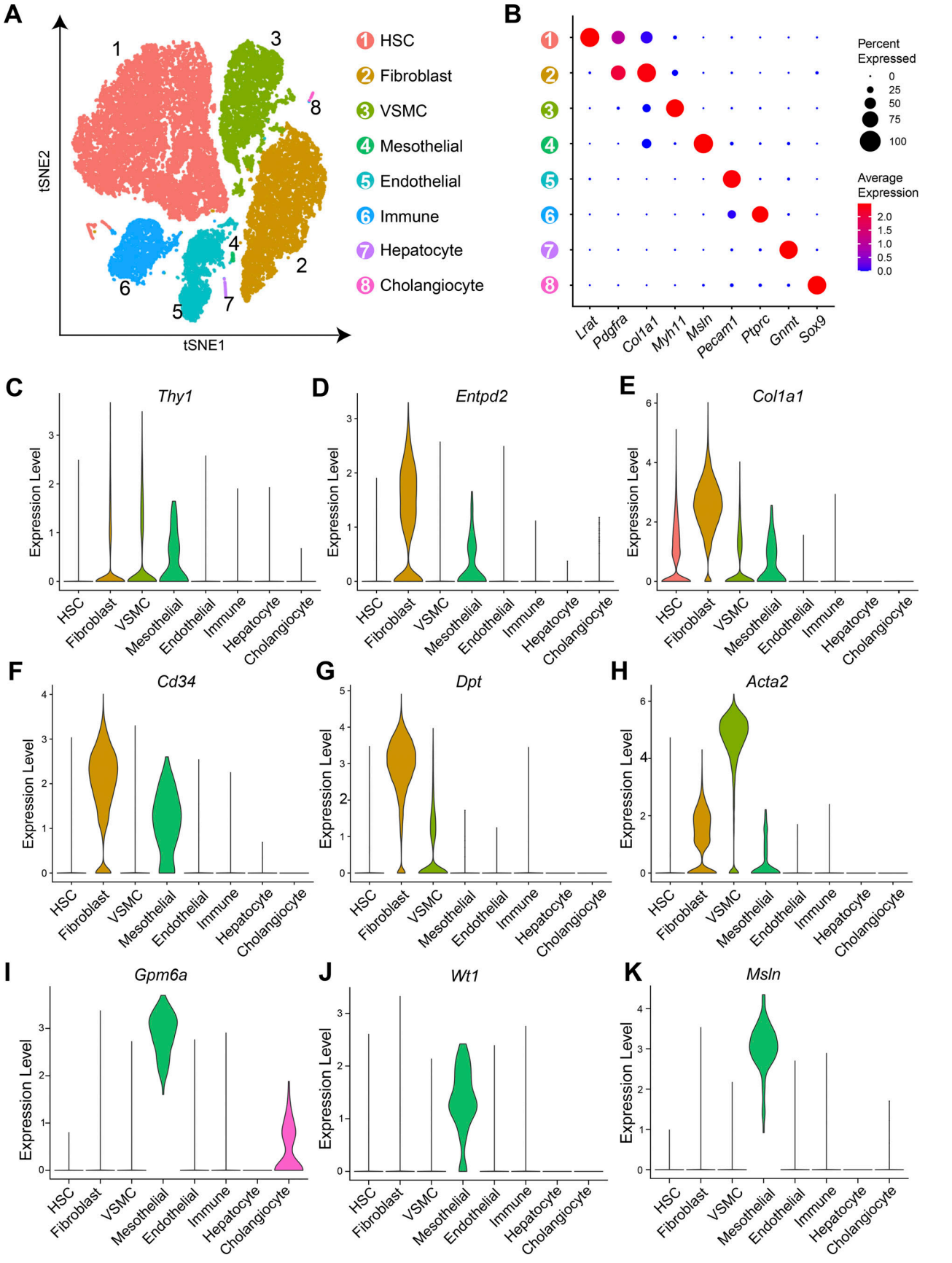

Figure 1. **Identification of potential markers for hepatic fibroblasts. (A)** Visualization of unsupervised clustering in a t-SNE plot of liver cells. **(B)** Dot plot showing the expression patterns of distinct cell type–specific marker genes in eight cell clusters. **(C–H)** Violin plots showing the expression levels of *Thy1*, *Entpd2*, *Col1a1*, *Cd34*, *Dpt*, *Acta2*, *Gpm6a*, *Wt1*, and *Msln* in different cell clusters.

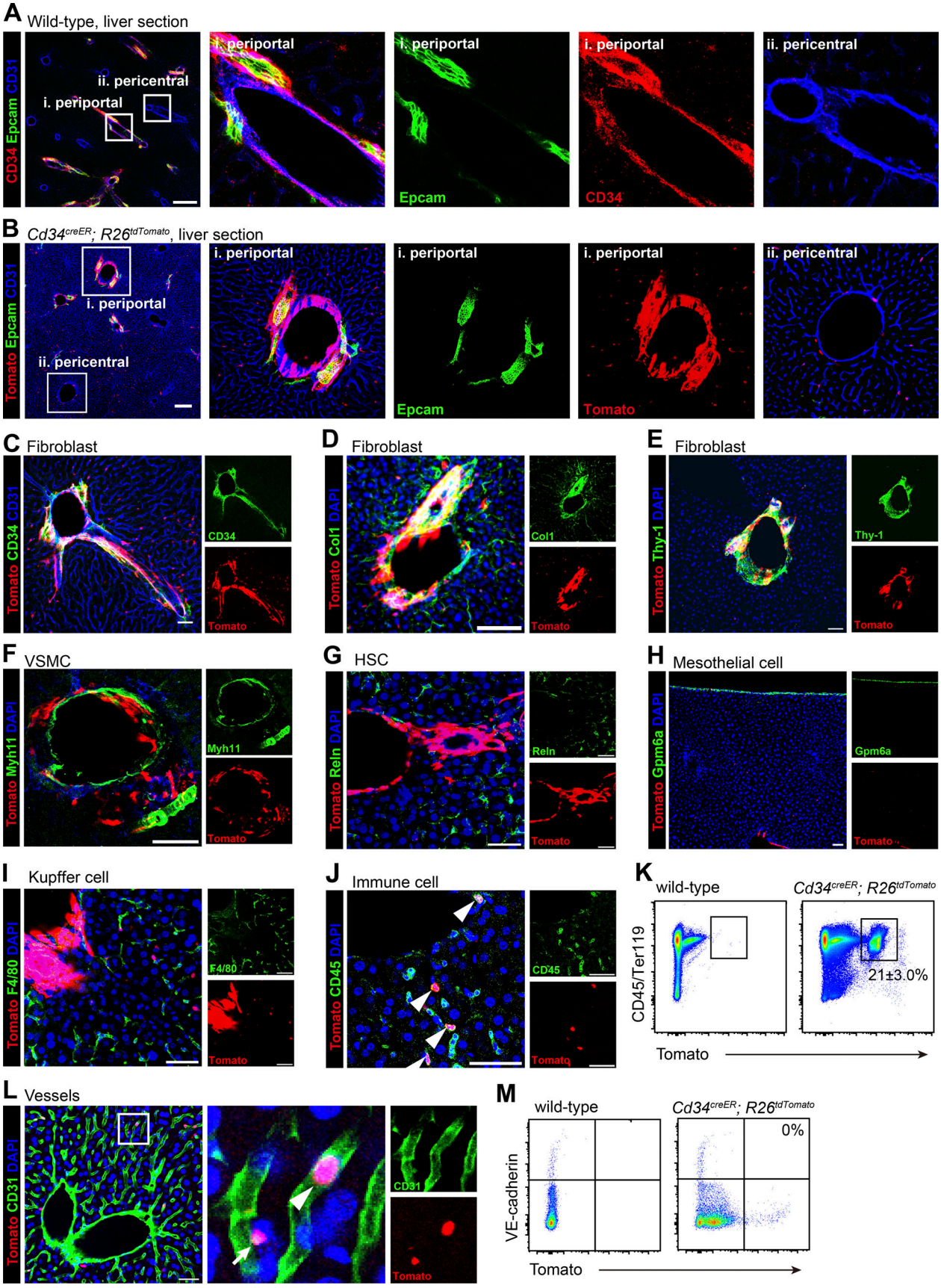

Figure 2. ***Cd34*-CreER labeled periductal and periportal-venous fibroblasts and a subset of immune cells, but not pericentral-venous fibroblasts, endothelial cells, or any other cell types in normal liver. (A)** Confocal images of liver sections (15 µm) showing the protein expression patterns of CD34.

Blood vessels and bile ducts were labeled by anti-CD31 and anti-Epcam antibodies, respectively. Scale bar = 200 µm (n = 3 mice from three independent experiments). All $Cd34^{creER};R26^{tdTomato}$ mice used in B–M were treated with tamoxifen for three consecutive days at 6 wk of age (n = 3–5 mice per condition from three independent experiments). **(B)** Confocal images showing Tomato expression in periductal and periportal-venous cells, but not pericentral-venous cells in $Cd34^{creER};R26^{tdTomato}$ livers. Blood vessels and bile ducts were labeled by anti-CD31 and anti-Epcam antibodies, respectively. Scale bar = 200 µm. **(C)** Confocal imaging revealed overlapping Tomato and CD34 expression (detected by anti-CD34 antibody) in the liver from 8-wk-old $Cd34^{creER};R26^{tdTomato}$ mice. Scale bar = 50 µm. **(D–I)** Confocal images showing Tomato expression in Col1$^+$ (D) and Thy-1$^+$ fibroblasts (E), but not in Myh11$^+$ VSMCs (F), Reln$^+$ HSCs (G), Gpm6a$^+$ mesothelial cells (H), or F4/80$^+$ Kupffer cells (I) in $Cd34^{creER};R26^{tdTomato}$ livers. Scale bar = 50 µm. **(J)** Confocal image showing Tomato expression in CD45$^+$ immune cells in $Cd34^{creER};R26^{tdTomato}$ livers. Scale bar = 50 µm. **(K)** Flow cytometric analysis showing the expression of Tomato in a subset of immune cells in the liver of $Cd34^{creER};R26^{tdTomato}$ mice. **(L)** Confocal image showing intravascular and extravascular localization of Tomato$^+$ cells in $Cd34^{creER};R26^{tdTomato}$ livers. Scale bar = 50 µm. Arrow depicts the extravascular Tomato$^+$ cell; arrowhead depicts the intravascular Tomato$^+$ cell. **(M)** Flow cytometric analysis showing that Tomato was not expressed in VE-cadherin$^+$ endothelial cells of $Cd34^{creER};R26^{tdTomato}$ mouse livers.

tamoxifen-treated $Cd34^{creER};R26^{tdTomato}$ mice by administration of CCl_4 twice per week for 4 wk. Successful induction of liver fibrosis was evidenced by Sirius red staining on paraffin sections (Fig. S3, A and B) and anti-Col1 staining on frozen sections (Fig. 3, A and B). Confocal analysis showed that there was no obvious expansion of Tomato$^+$ cells around the central veins of CCl_4-treated $Cd34^{creER};R26^{tdTomato}$ mice, compared with untreated controls (Fig. 3, A and B). Furthermore, few of the Col1$^+$ myofibroblasts formed after CCl_4 treatment expressed Tomato (Fig. 3, B and C), suggesting that *Cd34*-CreER$^+$ cells are not a source of myofibroblasts during CCl_4-induced pericentral fibrosis.

Biliary fibrosis was induced by 3,5-diethoxycarbonyl-1,4-dihydrocollidine (DDC) treatment. Successful induction of liver fibrosis was evidenced by Sirius red staining 14 days after treatment (Fig. S3 C). On liver sections from $Cd34^{creER};R26^{tdTomato}$ mice, we observed a marked increase of Tomato$^+$ cells around the portal triad (Fig. 3 D). By quantification, 25 ± 8.2% of all Col1$^+$ myofibroblasts formed 14 days after the treatment expressed Tomato (Fig. 3, D and E). These data suggested that *Cd34*$^+$ cells are a source of myofibroblasts in periportal fibrosis.

To determine the contribution of *Cd34*$^+$ cells to the CAF pool in liver tumors, we used an experimental mouse model of liver tumor formation. After a single injection of notch intracellular domain (NICD)/AKT plasmids at 8 wk of age, 100% of mice developed liver tumors by 5 wk (Fig. S3 D). Characteristics of ICC were observed in photographic comparisons of normal and tumorous livers (Fig. S3 D), H&E-stained sections (Fig. S3, E and F), and liver sections immunostained with anti-Sox9 and anti-Hnf4a antibodies, respectively (Fig. S3, G and H). By anti-Col1 staining, we detected CAFs throughout the tumoral tissue in $Cd34^{creER};R26^{tdTomato}$ mice (Fig. 3 F). Analysis of ICC livers from $Cd34^{creER};R26^{tdTomato}$ mice revealed that ∼40% of Col1$^+$ CAFs were Tomato$^+$ (Fig. 3, F and G), suggesting that *Cd34*$^+$ cells serve as a source of CAFs in ICC.

Dpt-CreER–labeled periportal-venous fibroblasts contributed to periportal fibrosis

In order to fate-map *Dpt*$^+$ fibroblasts, we generated Dpt^{creER} knock-in mice, in which a 2A ribosome "skipping" sequence fused with $creER^{T2}$ was inserted before the 3′UTR of the endogenous *Dpt* gene (Fig. S4 A). Dpt^{creER} mice were crossed with $R26^{tdTomato}$ mice to generate $Dpt^{creER};R26^{tdTomato}$ compound mutant mice. 2 wk after tamoxifen treatment, confocal imaging revealed robust Tomato expression around CD31$^+$ portal and central veins, much less around Epcam$^+$CD31$^-$ bile ducts, but not around CD31$^+$ sinusoids (Fig. 4 A). On liver sections, most of the Tomato$^+$ cells expressed the fibroblast markers Col1, Thy-1, and CD34, accounting for ∼12% of all CD34$^+$ fibroblasts (Fig. 4, B–D and Fig. S4 B), but not the SMC marker Myh11 (Fig. 4 E), the HSC marker Reln (Fig. 4 F), the mesothelial cell marker Gpm6a (Fig. 4 G), the hepatocyte marker Hnf4a (Fig. S4 F), or the Kupffer cell marker F4/80 (Fig. S4 G). On-slide staining of isolated non-parenchymal liver cells from $Dpt^{creER};R26^{tdTomato}$ mice detected Tomato expression in a subset of Col1$^+$ cells, but not Reln$^+$ or Myh11$^+$ cells (Fig. S4, C–E). Thus, *Dpt*-CreER specifically labels periportal- and pericentral-venous fibroblasts.

We investigated the potential contribution of *Dpt*-CreER–labeled cells to liver fibrosis. Pericentral fibrosis was induced in 2-mo-old tamoxifen-treated $Dpt^{creER};R26^{tdTomato}$ mice by administration of CCl_4, as described above. As a result, we did not observe a significant expansion of Tomato$^+$ cells in $Dpt^{creER};R26^{tdTomato}$ mice after CCl_4 treatment (Fig. 4 H). Furthermore, anti-Col1 immunostaining showed that only 1.8 ± 1.6% of all Col1$^+$ myofibroblasts were also Tomato$^+$ in the fibrotic livers (Fig. 4, H and I), indicating that *Dpt*-CreER–labeled cells do not contribute to pericentral fibrosis.

In the DDC-induced biliary liver periportal model, we observed expansion of Tomato$^+$ cells in the livers of $Dpt^{creER};R26^{tdTomato}$ mice (Fig. 4 J). Quantification of cell numbers showed that 15 ± 3.4% of all Col1$^+$DAPI$^+$ myofibroblasts were Tomato$^+$ in DDC-induced fibrosis (Fig. 4 K). Thus, *Dpt*-CreER–labeled cells are a source of myofibroblasts in periportal fibrosis.

We determined the contribution of *Dpt*-CreER–labeled cells to CAF formation in ICC. ICC was induced as described above. Analysis of liver sections revealed that only 2.5 ± 1.7% of all Col1$^+$ CAFs were Tomato$^+$ in ICCs of $Dpt^{creER};R26^{tdTomato}$ mice (Fig. 4, L and M), significantly lower than that in ICCs of $Cd34^{creER};R26^{tdTomato}$ mice (Fig. S4 H), suggesting that *Dpt*-CreER–labeled cells do not contribute to CAF formation in ICC.

Acta2-CreER–labeled VSMCs contributed minimally to myofibroblast and CAF formation

Co-staining with anti-CD31, anti-Epcam, and anti-aSma antibodies revealed the robust expression of aSma protein around the CD31$^+$ portal and central veins, but rarely around CD31$^+$ sinusoids or Epcam$^+$CD31$^-$ bile ducts (Fig. S4 I). To fate-map aSma$^+$ cells, we used *Acta2-creER* bacterial artificial chromosome transgenic mice, in which the $creER^{T2}$ coding sequence was inserted into a 175-kb mouse genomic segment encompassing

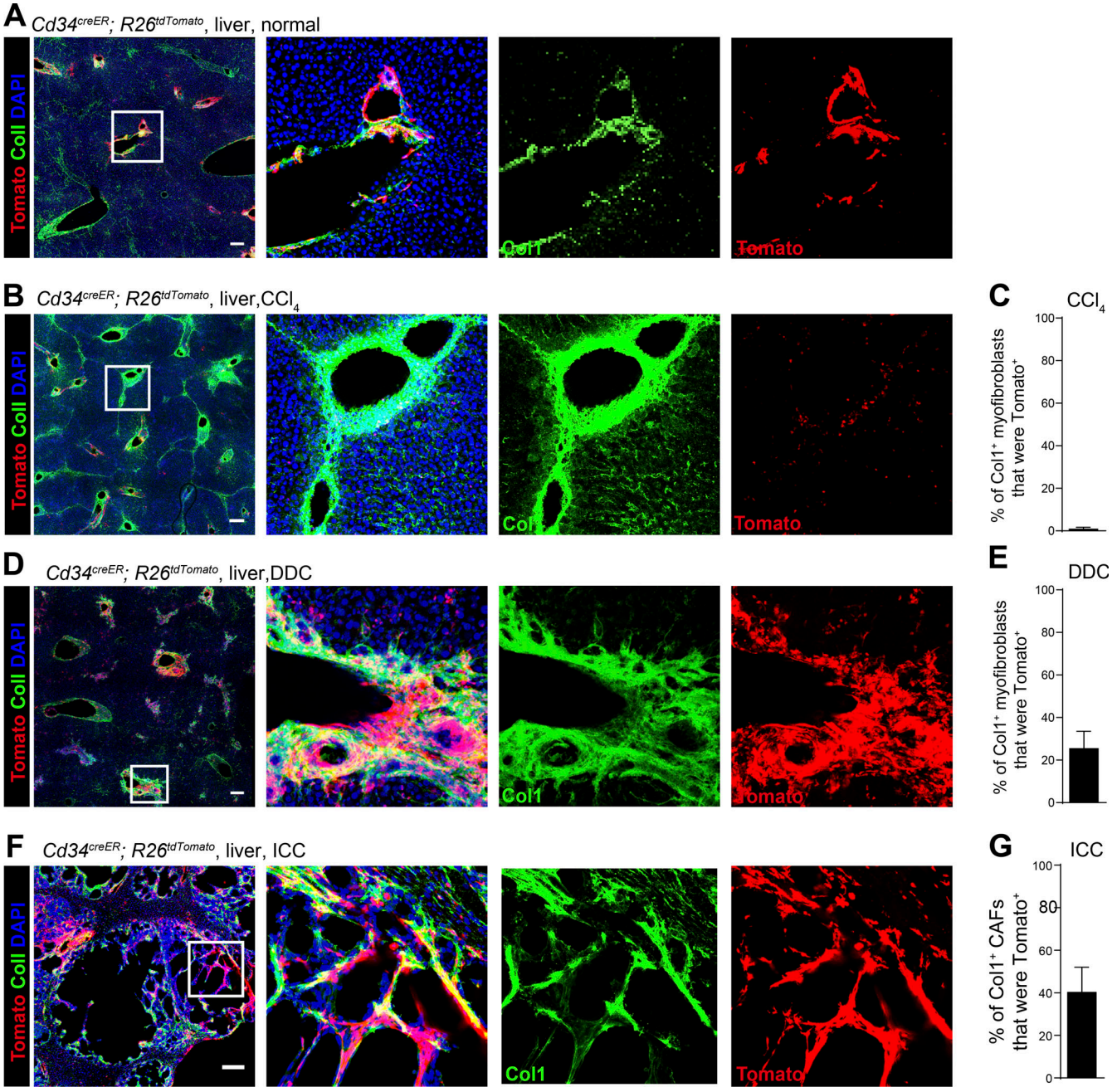

Figure 3. ***Cd34*⁺ cells generated myofibroblasts during periportal fibrosis and CAFs in ICC. (A, B, D, and F)** Confocal images of liver sections from normal (A), CCl_4-treated (B), DDC-treated (D), and ICC-bearing (F) *Cd34*^{creER};*R26*^{tdTomato} mice, stained with DAPI and anti-Col1 antibody. Scale bar = 200 µm (n = 5 mice per condition from three independent experiments). **(C, E, and G)** Quantification of the percentage of Col1⁺ cells that were Tomato⁺ in CCl_4-treated (C), DDC-treated (E), and ICC-bearing (G) *Cd34*^{creER};*R26*^{tdTomato} mice. Data represent the mean ± SD.

the *Acta2* gene (Wendling et al., 2009). Confocal imaging of anti-aSma antibody–stained liver sections confirmed specific and efficient recombination of *Acta2*-CreER in aSma⁺ cells from the liver of *Acta2-creER;R26*^{tdTomato} mice (Fig. 5 B). Co-staining of liver sections with anti-CD31 and anti-Epcam antibodies showed robust Tomato expression around CD31⁺ portal and central veins, but not around CD31⁺ sinusoids or Epcam⁺CD31⁻ bile ducts (Fig. 5 A). Most of the Tomato⁺ cells in the liver of *Acta2-creER;R26*^{tdTomato} mice were positive for Myh11 expression (Fig. 5 C). In contrast, Tomato⁺ liver cells poorly colocalized with anti-CD34 or anti-Col1 staining (Fig. 5, D and E). The Tomato⁺ cells and Col1⁺ fibroblasts appeared to localize at different layers of the portal veins and arteries (Fig. S4, J and K). Tomato expression was not detected in Reln⁺ HSCs, F4/80⁺ Kupffer cells, or Hnf4a⁺ hepatocytes (Fig. 5, F and G; and Fig. S4 L). These data suggested that *Acta2*-CreER labels VSMCs rather than fibroblasts. Considering the high expression of *Acta2* mRNA in VSMCs and moderate expression in fibroblasts (Fig. 1 H), the moderate expression of *Acta2* in fibroblasts appeared insufficient to activate Cre expression.

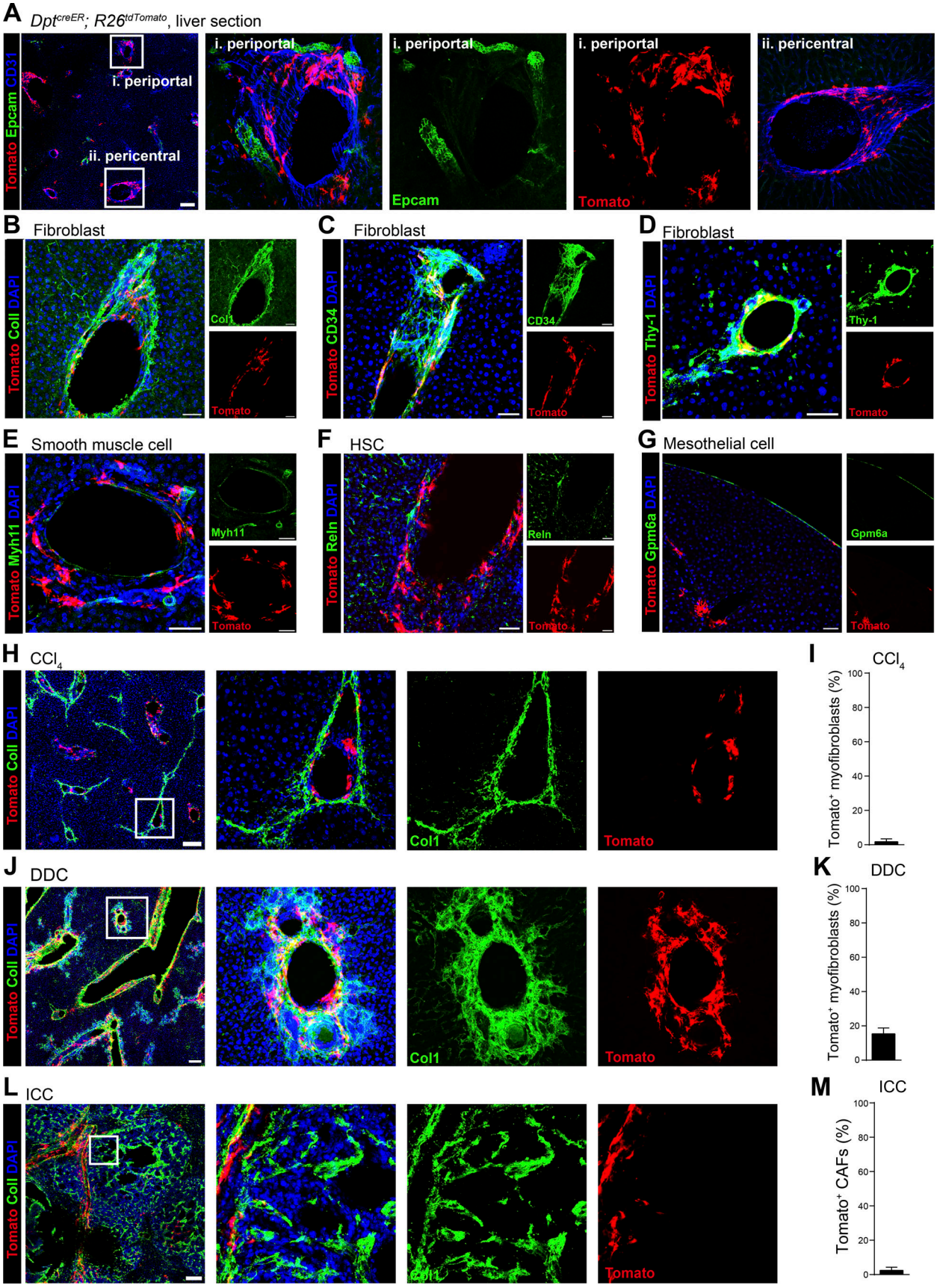

Figure 4. ***Dpt*-CreER–labeled periportal-venous fibroblasts contributed to periportal fibrosis.** All Dpt^{creER};$R26^{tdTomato}$ mice used in A–L were treated with tamoxifen for three consecutive days at 6 wk of age (n = 3–5 mice per condition from three independent experiments). **(A)** Confocal images showing Tomato

expression in pericentral- and periportal-venous cells but rare in periductal cells of 8-wk-old *Dpt*^{creER};*R26*^{tdTomato} livers. Blood vessels and bile ducts were labeled by anti-CD31 and anti-Epcam antibodies, respectively. Scale bar = 200 µm. **(B–G)** Confocal images showing Tomato expression in Col1$^+$ (B), CD34$^+$ (C), and Thy-1$^+$ fibroblasts (D), but not in Myh11$^+$ VSMCs (E), Reln$^+$ HSCs (F), or Gpm6a$^+$ mesothelial cells (G) of *Dpt*^{creER};*R26*^{tdTomato} livers. Scale bar = 50 µm. **(H–M)** Confocal images of liver sections from CCl_4-treated (H), DDC-treated (J), and ICC-bearing (L) *Dpt*^{creER};*R26*^{tdTomato} mice, stained with DAPI and anti-Col1 antibody. Scale bar = 200 µm. Data represent the mean ± SD (I, K, and M).

To further investigate the expression patterns of *Cd34*-CreER, *Dpt*-CreER, and *Acta2*-CreER in VSMCs, fibroblasts, and HSCs, we sorted Tomato$^+$CD45$^-$ cells from the livers of *Tcf21*^{creER};*R26*^{tdTomato} mice, *Cd34*^{creER};*R26*^{tdTomato} mice, *Dpt*^{creER};*R26*^{tdTomato} mice, and *Acta2-creER;R26*^{tdTomato} mice, respectively, and examined their expression of *Col1a1*, *Cd34*, *Myh11*, and *Reln*. We have shown that *Tcf21*-CreER labels HSCs (Wang et al., 2021). As a result, Tomato$^+$ cells from *Cd34*^{creER};*R26*^{tdTomato} and *Dpt*^{creER};*R26*^{tdTomato} mice expressed robust levels of *Col1a1* and *Cd34*, but not *Myh11* or *Reln* (Fig. S5). In contrast, Tomato$^+$ cells from *Acta2-creER;R26*^{tdTomato} mice expressed robust levels of *Myh11*, but not *Col1a1*, *Cd34*, or *Reln* (Fig. S5). These data confirmed the specific expression of *Cd34*-CreER and *Dpt*-CreER in fibroblasts and *Acta2*-CreER in VSMCs.

We investigated the potential contribution of *Acta2*-CreER–labeled cells to myofibroblast formation in liver fibrosis and CAF formation in ICC. The results showed that *Acta2*-CreER–labeled cells generated 1.1 ± 0.84% and 2.1 ± 2.1% of all Col1$^+$ myofibroblasts formed in CCl_4- and DDC-induced fibrosis, respectively (Fig. 5, H–K). In ICC, they generated 1.7 ± 1.6% of all Col1$^+$ CAFs (Fig. 5, L and M). Thus, *Acta2*-CreER–labeled cells contribute minimally to myofibroblast formation in liver fibrosis and CAF formation in ICC.

Depletion of *Cd34*$^+$ cells promoted cholangiocyte proliferation and ICC progression

To determine the physiological importance of the fibroblast in the liver, we crossed *Cd34*^{creER} mice with *R26*$^{CAG\text{-}loxp\text{-}STOP\text{-}lox\text{-}DTA}$ (*R26*^{DTA}) mice to generate a strain in which Cre-expressing cells and their descendants would be constitutively depleted by the expression of diphtheria toxin (Voehringer et al., 2008). Cre expression was induced in *Cd34*^{creER};*R26*^{DTA} compound mutants at 6 wk of age, as above, and the mice were analyzed at 8 wk. Confocal imaging confirmed the efficient depletion of Tomato$^+$ cells from the liver of *Cd34*^{creER};*R26*$^{tdTomato/DTA}$ mice upon tamoxifen treatment (Fig. 6, A and B). H&E staining on paraffin sections did not reveal obvious changes to liver morphology in *Cd34*^{creER};*R26*^{DTA} mice, compared with *R26*^{DTA} mice (Fig. S5 E). However, staining of the ductal epithelium by anti-Sox9 antibody revealed that the bile ducts were enlarged in diameter and the number of cholangiocytes lining the bile ducts was significantly increased. In normal liver, intrahepatic bile ducts were lined by four to eight cholangiocytes (except for the large intrahepatic bile ducts lining the primary portal vein), whereas in livers from *Cd34*^{creER};*R26*^{DTA} mice, bile ducts were lined by 6 to 10 cholangiocytes (Fig. 6, C and D). These findings indicated that depletion of *Cd34*$^+$ cells resulted in enlargement of the bile ducts.

We administered 5-ethynyl-2′-deoxyuridine (EdU) to *Cd34*^{creER};*R26*^{DTA} and *R26*^{DTA} control mice immediately after tamoxifen treatment to directly assess cholangiocyte proliferation following depletion of *Cd34*$^+$ cells. After 4 wk, we found that ∼38% of all Epcam$^+$ cholangiocytes were EdU-positive in *Cd34*^{creER};*R26*^{DTA} mice, which was significantly higher compared with about 16% in *R26*^{DTA} control mice (Fig. 6, E and F). This indicates a marked increase in cholangiocyte proliferation following the depletion of *Cd34*$^+$ cells. In contrast, there was no significant difference in the overall percentage of EdU$^+$ cells across the liver tissue between the two groups (Fig. 6, E and F), suggesting that the observed effects were specific to cholangiocytes.

Next, we subjected tamoxifen-treated *Cd34*^{creER};*R26*^{DTA} mice and littermate *R26*^{DTA} mice to DDC-induced liver fibrosis. Livers from all mice exhibited clear liver fibrotic phenotypes, as revealed by Sirius red staining (Fig. 6 G). We did not detect a significant difference between *Cd34*^{creER};*R26*^{DTA} and *R26*^{DTA} mice with respect to the percentage of liver area stained by Sirius red (Fig. 6 H). Consistent with this, the mRNA levels of *Col1* and *Acta2* in fibrotic livers from *Cd34*^{creER};*R26*^{DTA} and *R26*^{DTA} mice did not significantly differ from each other (Fig. 6, I and J). These data suggested that conditional depletion of *Cd34*$^+$ cells does not affect biliary fibrosis.

We conditionally deleted *Tgfbr2* from *Cd34*$^+$ cells to determine the requirement of Tgfβ signaling in myofibroblast formation by portal fibroblasts. We performed DDC treatment on both control and mutant mice. After 2 wk, we detected significantly less Tomato$^+$Col1$^+$ myofibroblasts in *Cd34*^{creER};*R26*^{tdTomato};*Tgfbr2*$^{fl/fl}$ mice than in control mice, despite that the overall Col1$^+$ myofibroblasts did not differ between control and mutant mice (Fig. 6, K and L). Thus, the formation of myofibroblasts by *Cd34*$^+$ fibroblasts requires Tgfβ signaling.

We also subjected tamoxifen-treated *Cd34*^{creER};*R26*^{DTA} mice and *R26*^{DTA} littermates to ICC induction. At 3 wk after plasmid injection, the percentage of tumor area was significantly greater in *Cd34*^{creER};*R26*^{DTA} liver than in *R26*^{DTA} liver (Fig. 6, M and N). In contrast, at 4 wk after plasmid injection, there was no significant difference between *Cd34*^{creER};*R26*^{DTA} and *R26*^{DTA} mice with respect to the percentage of tumor area within the liver (Fig. 6, O and P). Consistent with this, the mRNA levels of *Col1* and *Acta2* in ICC livers from *Cd34*^{creER};*R26*^{DTA} mice were significantly higher than those from *R26*^{DTA} mice at 3 wk, but not at 4 wk, after plasmid injection (Fig. 6, Q and R). These data suggested that conditional depletion of *Cd34*$^+$ cells accelerated the progression of ICC.

Cd34-CreER–labeled bone marrow cells do not contribute to liver fibrosis or ICC

We transplanted bone marrow cells from *Cd34*^{creER};*R26*^{tdTomato} mice into lethally irradiated wild-type mice. 8 wk after transplantation, we detected many Tomato$^+$ immune cells, but no Tomato$^+$ fibroblasts in the liver of the recipients (Fig. 7, A and B).

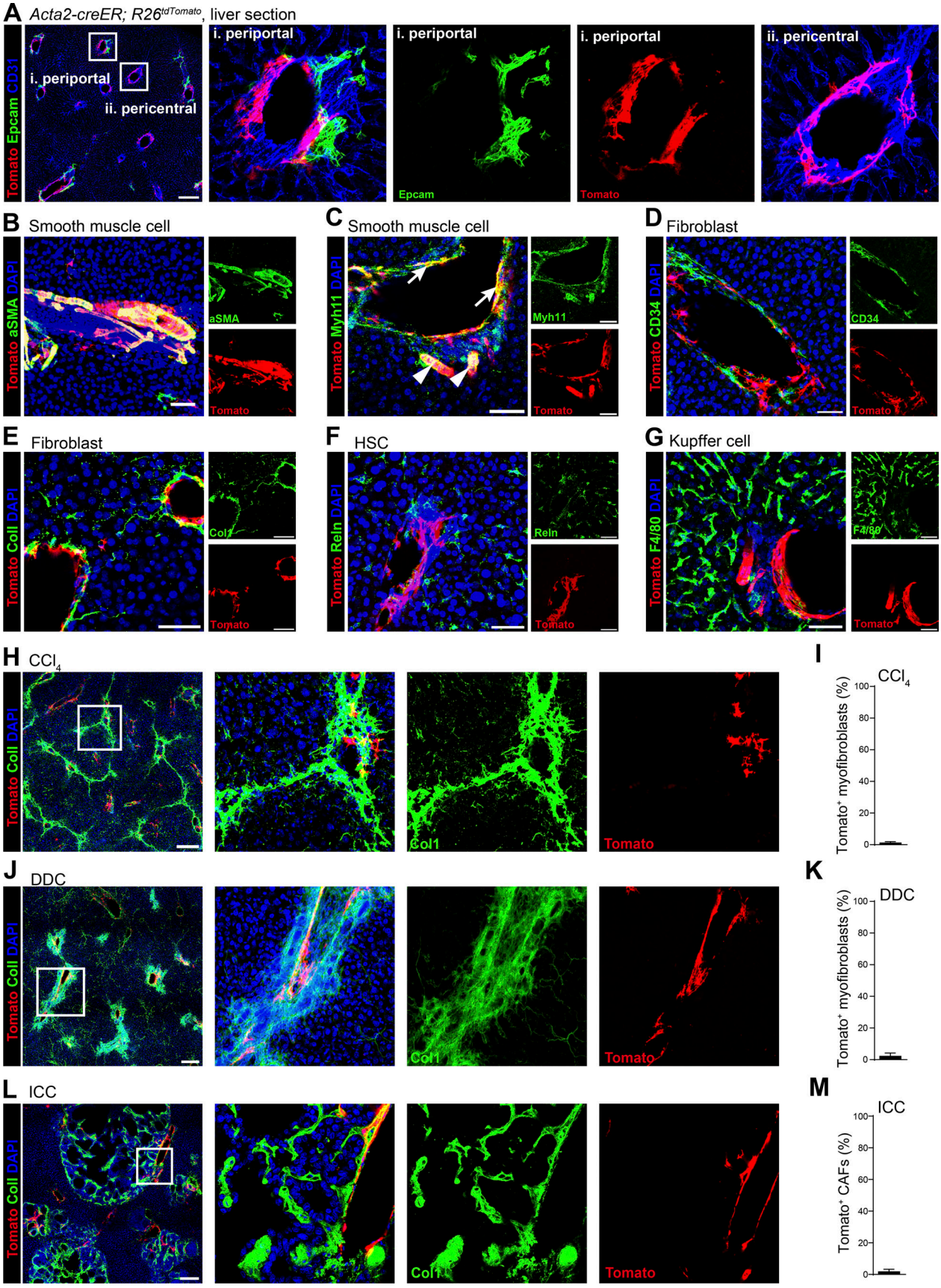

Figure 5. ***Acta2*-CreER–labeled VSMCs contributed minimally to myofibroblasts and CAFs.** All *Acat2-creER;R26*^{tdTomato} mice used in A–M were treated with tamoxifen for three consecutive days at 6 wk of age and analyzed at 8 wk of age (n = 3–5 mice per condition from three independent experiments).

(A) Confocal images showing Tomato expression in pericentral- and periportal-venous cells, but not in periductal or perisinusoidal cells of *Acta2-creER;R26*^{tdTomato} livers. Blood vessels and bile ducts were labeled by anti-CD31 and anti-Epcam antibodies, respectively. Scale bar = 200 µm. **(B)** Confocal imaging revealed overlapping Tomato and aSma expression (detected by anti-aSma antibody) in the liver from *Acta2-creER;R26*^{tdTomato} mice. Scale bar = 50 µm. **(C–G)** Confocal images showing Tomato expression in Myh11$^+$ VSMCs (C), but not in CD34$^+$ (D) or Col1$^+$ fibroblasts (E), Reln$^+$ HSCs (F), or F4/80$^+$ Kupffer cells (G) in *Acta2-creER;R26*^{tdTomato} livers. Arrows and arrowheads indicated VSMCs at portal veins and arteries, respectively (C). Please see Fig. S4 J for a magnified view of E. Scale bar = 50 µm. **(H–M)** Confocal images of liver sections from CCl_4-treated (H and I), DDC-treated (J and K), and ICC-burdened (L and M) *Acta2-creER;R26*^{tdTomato} mice, stained with DAPI and anti-Col1 antibody. Scale bar = 200 µm. Data represent the mean ± SD (I, K, and M).

After DDC treatment for another 2 wk, we did not detect any Tomato$^+$ myofibroblasts in the fibrotic liver (Fig. 7 C). At 4 wk after ICC induction, we did not detect any Tomato$^+$ CAFs in the tumor (Fig. 7 D). These data excluded the possibility that *Cd34*-CreER–labeled immune cells contribute to liver fibrosis or ICC.

We also transplanted bone marrow cells from wild-type mice into lethally irradiated *Cd34*^{creER}*;R26*^{tdTomato}, *Cd34*^{creER}*;R26*^{DTA}, and *R26*^{DTA} control mice. 8 wk after transplant, we induced Tomato or DTA expression using tamoxifen. Confocal imaging of liver sections from *Cd34*^{creER}*;R26*^{tdTomato} recipients showed that CD45$^+$ immune cells no longer expressed Tomato, confirming that hematopoietic cells were effectively replaced and did not contribute to the observed phenotypes (Fig. 7, E and F). Further analysis of bile duct morphology through anti-Sox9 staining revealed that bile ducts were significantly enlarged, and the number of cholangiocytes lining the ducts was increased in *Cd34*^{creER}*;R26*^{DTA} recipients compared with *R26*^{DTA} controls (Fig. 7, G and H), replicating phenotypes observed in non-transplanted settings. When inducing ICCs in *Cd34*^{creER}*;R26*^{DTA} and *R26*^{DTA} recipients, the tumor area was significantly greater in *Cd34*^{creER}*;R26*^{DTA} recipients than in *R26*^{DTA} controls at 3 wk after induction (Fig. 7, I and J). These findings demonstrated that the effects seen are attributable to the depletion of *Cd34*$^+$ fibroblasts, not hematopoietic cells.

Discussion

In this study, we used *Cd34*-CreER, *Dpt*-CreER, and *Acta2*-CreER mice to trace fibroblasts and VSMCs in the liver under various conditions. An ontological combination of *Cd34*-CreER and *Dpt*-CreER distinguished the fates of periductal, periportal-, and pericentral-venous fibroblasts. Hepatic fibroblasts are a heterogeneous population and have been implicated in liver homeostasis and diseases (Dranoff and Wells, 2010; Lemoinne et al., 2015; Wells, 2014). Most previous studies have focused on the fibroblasts surrounding the portal triad, although fibroblasts are also present around the central veins and in the liver capsule beneath the mesothelium (Bhunchet and Wake, 1992; Chapman and Eagles, 2007). scRNA-seq studies have identified several groups of fibroblast subpopulations derived from the biliary–vascular tree, among which the *Pdgfra*$^+$*Cd34*$^+$*CD9*$^+$*CD200*^{low} subpopulation conferred mesenchymal stem cell features in vitro (Lei et al., 2022). Our work has revealed that *Cd34*$^+$*Dpt*$^-$ periductal fibroblasts contributed to ductal homeostasis, biliary fibrosis, and tumorigenesis. *Cd34*$^+$*Dpt*$^+$ periportal-venous fibroblasts contribute to biliary fibrosis. *Cd34*$^-$*Dpt*$^+$ pericentral-venous fibroblasts do not contribute to pericentral fibrosis.

HSCs are a major source of myofibroblasts in multiple models of biliary liver fibrosis (Mederacke et al., 2013; Wang et al., 2021) and are also likely to represent the main source of stromal cell–derived CAFs in liver tumors (Brivio et al., 2017; Wang et al., 2021). Our fate-mapping results showed that fibroblasts marked by *Cd34*-CreER contributed to ∼25% of all myofibroblasts in biliary fibrosis (Fig. 3, D and E). However, it was notable that conditional depletion of these cells did not impair liver fibrosis (Fig. 6, G–J). We speculated that HSCs compensate for the loss of *Cd34*$^+$ cells by producing additional myofibroblasts. Mesothelial cells have been shown to be involved in capsular fibrosis (Balog et al., 2020), suggesting a division-of-labor among different stromal cells in myofibroblast formation in different types of liver fibrosis. We also showed that conditional depletion of *Cd34*$^+$ fibroblasts accelerated the progression of ICC (Fig. 6, M–R). One possible mechanism is that *Cd34*$^+$ periductal fibroblasts restrict the proliferation of cholangiocytes (Fig. 6, C and D), the cell type from which ICCs arise. This finding is in line with the negative role of fibroblasts in ductal epithelial cell proliferation in a mesenchymal-ductal organoid co-culture system (Cordero-Espinoza et al., 2021). Another mechanism could be a direct regulation of tumor cell proliferation by *Cd34*$^+$ fibroblasts in ICC, potentially through the secretion of antitumorigenic factors.

Increasing evidence has demonstrated the heterogeneity of the CAF compartment in liver tumors. Different CAF subpopulations may play distinct or even opposing roles in the formation and/or progression of liver tumors (Affo et al., 2021; Filliol et al., 2022). We have shown that *Cd34*$^+$ fibroblasts form a significant proportion (∼40%) of all CAFs in a mouse model of ICC (Fig. 3, F and G). While our current study design did not allow for a detailed investigation into whether CD34$^+$ fibroblasts contribute to specific subtypes of CAFs, this remains an intriguing possibility for future research.

Materials and methods

Mice

All mice strains, including *R26*^{tdTomato} (Madisen et al., 2010), *Acta2-creER* (Wendling et al., 2009), *Cd34*^{creER}, *Dpt*^{creER}, *R26*^{DTA} (Voehringer et al., 2008), and *Tgfbr2*^{fl} mice (Chytil et al., 2002), were housed in the animal facility at Shanghai Institute of Biochemistry and Cell Biology (SIBCB). Construction of *Cd34*^{creER} and *Dpt*^{creER} mice was performed by Shanghai Biomodel Organism Co., Ltd. *Cd34*^{creER} was generated by knocking *creER* into the ATG site of the endogenous *Cd34* gene. *Dpt*^{creER} was generated by knocking 2A-*creER* before the 3′UTR of the endogenous *Dpt* gene. To induce CreER activity, intraperitoneal injections of 2 mg tamoxifen (Sigma-Aldrich) dissolved in corn oil were administered daily for three consecutive days. All procedures were approved by the Institutional Animal Care and Use Committee of SIBCB.

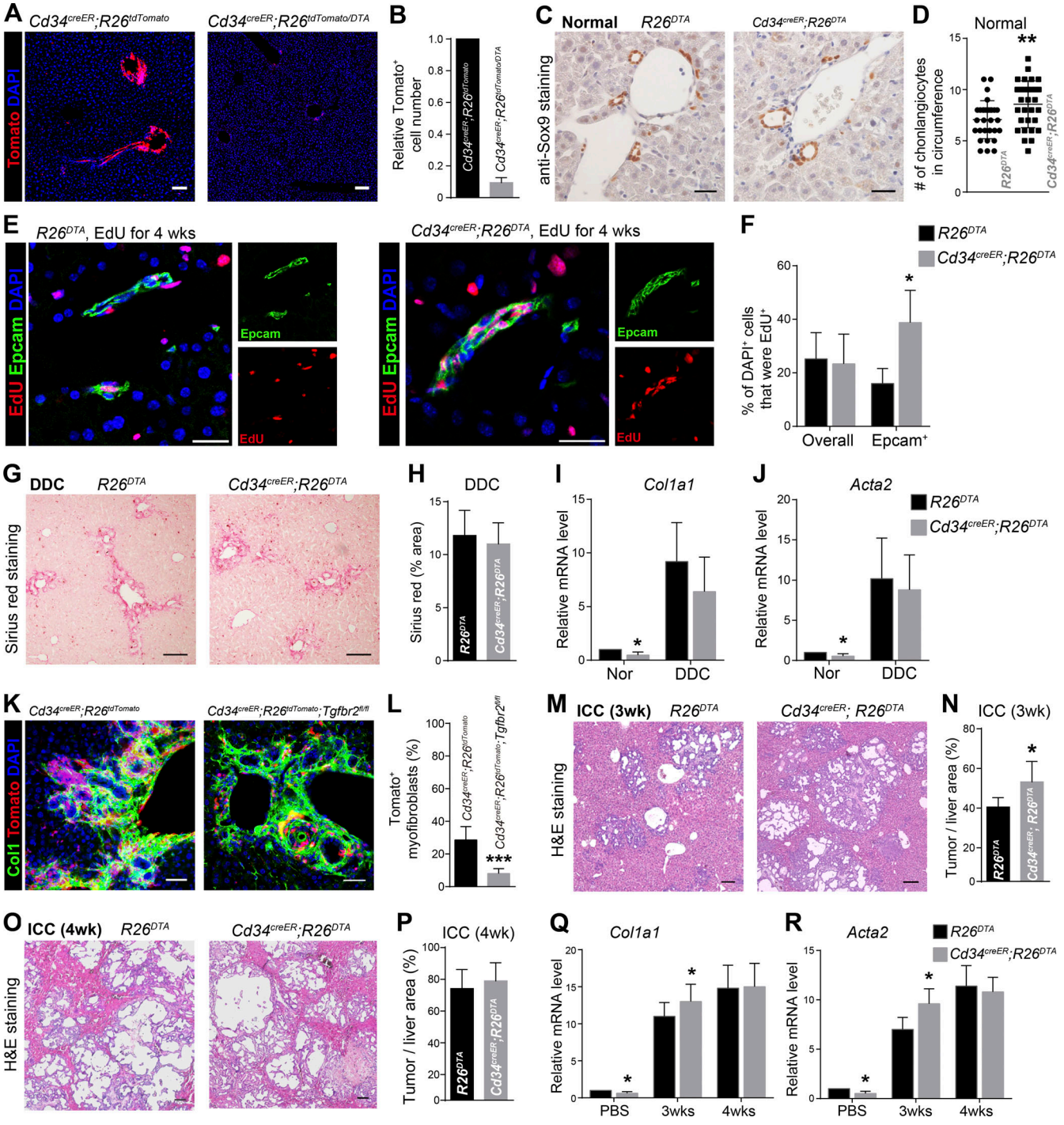

Figure 6. **Depletion of *Cd34*⁺ cells affected ductal homeostasis and tumorigenesis. (A)** Confocal images of liver sections from 8-wk-old *Cd34*^{creER};*R26*^{tdTomato} and *Cd34*^{creER};*R26*$^{DTA/tdTomato}$ mice that had been treated with tamoxifen at 6 wk of age. Scale bar = 100 µm. **(B)** Numbers of Tomato⁺ cells in *Cd34*^{creER};*R26*$^{DTA/tdTomato}$ liver sections were quantified relative to the numbers of Tomato⁺ cells in *Cd34*^{creER};*R26*^{tdTomato} liver sections (n = 5 mice per genotype from three independent experiments). **(C and D)** Anti-Sox9 staining of paraffin liver sections (C) from 8-wk-old *R26*^{DTA} and *Cd34*^{creER};*R26*^{DTA} mice treated with tamoxifen at 6 wk of age. Scale bar = 50 µm. The numbers of Sox9⁺ cholangiocytes forming the circumference of the bile ducts were quantified (D) (n = 5 mice per genotype from three independent experiments). **(E and F)** EdU incorporation of *R26*^{DTA} and *Cd34*^{creER};*R26*^{DTA} mice in a period of 4 wk right after tamoxifen administration. Cholangiocytes were revealed by anti-Epcam staining (E). The percentages of all DAPI⁺ cells and DAPI⁺Epcam⁺ cells that incorporated EdU were quantified (F). Scale bar = 25 µm (n = 5 mice per genotype from three independent experiments). **(G and H)** Sirius red staining of paraffin liver sections (G) from DDC-treated *R26*^{DTA} and *Cd34*^{creER};*R26*^{DTA} mice (pretreated with tamoxifen at 6 wk of age). DDC treatment was started at 8 wk of age. Scale bar = 100 µm. The percentage of Sirius red–stained tissue within liver sections was quantified (H) (n = 5 mice per genotype from three independent experiments). **(I and J)** Relative mRNA levels of *Col1a1* (I) and *Acta2* (J) in non-parenchymal liver cells from *R26*^{DTA} and *Cd34*^{creER};*R26*^{DTA} mice under normal conditions or after DDC treatment. The mRNA level in *R26*^{DTA} mice under normal conditions was set as 1. Data represent the mean ± SD (n = 5 mice per genotype from three independent experiments). **(K and L)** Confocal images of liver sections from DDC-treated *Cd34*^{creER};*R26*^{tdTomato} and *Cd34*^{creER};*R26*^{tdTomato};*Tgfbr2*$^{fl/fl}$ mice, stained

with DAPI and anti-Col1 antibody (K). Scale bar = 50 µm. Data represent the mean ± SD (L) (n = 5 mice per genotype from three independent experiments). **(M–P)** H&E staining of paraffin liver sections (M and O) from ICC-bearing $R26^{DTA}$ and $Cd34^{creER};R26^{DTA}$ mice (pretreated with tamoxifen at 6 wk of age). ICC was induced at 8 wk of age. Scale bar = 200 µm. The percentage of tumor area within liver sections was quantified (N and P) (n = 5 mice per genotype from three independent experiments). **(Q and R)** Relative mRNA levels of *Col1a1* (Q) and *Acta2* (R) in non-parenchymal liver cells from $R26^{DTA}$ and $Cd34^{creER};R26^{DTA}$ mice under normal conditions or after ICC induction. The mRNA level in $R26^{DTA}$ mice under normal conditions was set as 1. Data represent the mean ± SD (n = 5 mice per condition from three independent experiments). The statistical significance of differences was always assessed by two-tailed Student's t tests. *P < 0.05, **P < 0.01, ***P < 0.001.

Induction of liver fibrosis

To induce pericentral liver fibrosis, CCl_4 (Sigma-Aldrich) dissolved in corn oil (1:4) was injected intraperitoneally at a dose of 1 µl per gram body weight biweekly for 4 wk. To induce biliary fibrosis, 8–12-wk-old mice were fed on a diet supplemented with 0.1% DDC (D17142193; Future Biotech) for 2–4 wk.

Induction of ICC

ICC was induced according to the literature (Fan et al., 2012). Briefly, 20 µg pT3-EF1a-NICD1, 4 µg pT3-EF1a-HA-myr-Akt, and 1 µg transposase plasmids were diluted in 2 ml 0.9% NaCl, sterile-filtered, and administered to 6–8-wk-old mice by hydrodynamic tail vein injection.

Immunohistochemistry

Mouse livers were fixed in 4% paraformaldehyde (PFA) overnight, dehydrated through an ethanol series (70%, 80%, 95%, 100%), embedded in paraffin, cut into 5-µm sections using the Leica manual rotary microtome (Leica Biosystems), and placed on adhesion microscope slides (Xinyu Biotech). After dewaxing and hydration, liver sections were stained with Sirius red or hematoxylin and eosin (H&E) and mounted on slides for imaging by a BX51 (Olympus) microscope.

Immunostaining

Liver samples were fixed overnight in 4% PFA at 4°C, dehydrated in 30% sucrose for 24 h, embedded in OCT (NEG-50-6502; Thermo Fisher Scientific), and then cut into 15-µm sections using a cryostat microtome (Leica Biosystems). Sections were incubated with primary antibodies overnight at 4°C and then washed three times in PBS. After 2 h of incubation with secondary antibodies at room temperature, sections were washed in PBS and mounted on slides using ProLong Gold Antifade Reagent (Invitrogen). Images were captured by a Leica TCS SP8 WLL or a Leica TCS SP8 STED confocal microscope. Antibodies were diluted in PBS containing 10% donkey serum and 0.1% Triton X-100. The following primary antibodies were used: anti-aSma (1:250, ab5694; Abcam), anti-CD31 (1:250, AF3628; R&D), anti-F4/80 (1:250, MCA497rt; Bio-Rad), anti-CD34 (1:100, ab81289; Abcam), anti-Reln (1:100, AF3820; R&D), anti-Col1 (1:200, A1352; ABclonal), anti-Myh11 (1:100, HPA015310; Atlas Antibodies), and anti-Hnf4a (1:500, ab181604; Abcam). The following secondary antibodies were used: donkey anti-rabbit Alexa Fluor 647 (1:500, A31573; Invitrogen), donkey anti-goat Alexa Fluor 488 (1:500, A21432; Invitrogen), donkey anti-rat Alexa Fluor 488 (1:500, A21208; Invitrogen), donkey anti-rabbit Alexa Fluor 488 (1:500, A21206; Invitrogen), donkey anti-goat Alexa Fluor 647 (1:500, A21447; Invitrogen), and donkey anti-goat BV421 (1:200, 705-675-147; Jackson ImmunoResearch).

Flow cytometry

To prepare liver cells for flow cytometry, mouse liver was digested according to a previously published protocol (Mederacke et al., 2015). Briefly, after cannulation of the inferior vena cava, the portal vein was cut to allow retrograde stepwise perfusion of Liver Perfusion Medium (17701038; Gibco) for 5 min, followed by pronase (0.4 mg/ml, 5 min, 10165921001; Sigma-Aldrich)- and collagenase type IV (1 mg/ml, 15 min, 17104019; Gibco)–containing HBSS. Livers were then excised and minced, before ex vivo digestion in HBSS containing 0.5 mg/ml pronase, 1 mg/ml collagenase types I and IV, and 1 mg/ml DNase I (11284932001; Sigma-Aldrich). Cells were stained with CD144 (VE-cadherin)-BV421 (1:100, 747749; BD), CD45-APC (1:200, 103112; BioLegend), and Ter119-APC (1:200, 116212; BioLegend) antibodies for 30 min. To prepare bone marrow cells, bone cavities were flushed using a syringe containing 1 ml buffer (HBSS with 2% FBS). Cells were stained with lineage mix on ice for 30 min: Ter119-APC780 (1:200, 47-5921-82; eBioscience), CD3-APC780 (1:200, 47-0031-82; eBioscience), CD5-APC780 (1:200, 47-0051-82; eBioscience), CD8a-APC780 (1:200, 47-0081-82; eBioscience), B220-APC780 (1:200, 47-0452-82; eBioscience), Gr-1-APC780 (1:400, 47-5931-82; eBioscience), Sca1(Ly6a)-PerCPcy5.5 (1:100, 122524; BioLegend), CD117(c-Kit)-BV421 (1:200, 105828; BioLegend), CD48-APC (1:200, 103412; BioLegend), and CD150-PEcy7 (1:100, 115914; BioLegend). Flow cytometry was performed on a BD LSRFortessa flow cytometry system, and data were analyzed using FlowJo software.

Non-parenchymal cell isolation and on-slide immunostaining

After enzymatic digestion of the liver from $Cd34^{creER};R26^{tdTomato}$ mice, non-parenchymal cells were isolated from the interface between the two density cushions of 25% and 50% Percoll (P4937-500 Ml; Sigma-Aldrich) by gradient centrifugation (1,500 g for 20 min). Isolated cells were fixed with 4% PFA for 20 min, permeabilized with 0.5% Triton X-100 for another 20 min, and blocked with 5% BSA for an hour. They were then mounted on poly-D-lysine–coated slides and incubated with antibodies as indicated.

EdU incorporation assay

$Cd34^{creER};R26^{DTA}$ and $R26^{DTA}$ control mice were fed with EdU (0.5 mg/ml in the water supply) for 4 wk right after tamoxifen induction. To detect EdU incorporation, liver sections wer; Carbosynthe incubated with EdU labeling cocktail containing 2.5 µM sulfo-Cyanine5 azide (Abcam) for 20 min. Confocal microscopy was performed as described above.

Liver clearing and 3D imaging

Liver lobes were fixed in 4% PFA at room temperature for 24 h and then cleared using the PEGASOS method (Jing et al., 2018). Briefly, the liver lobes were treated with 25% Quadrol (122262;

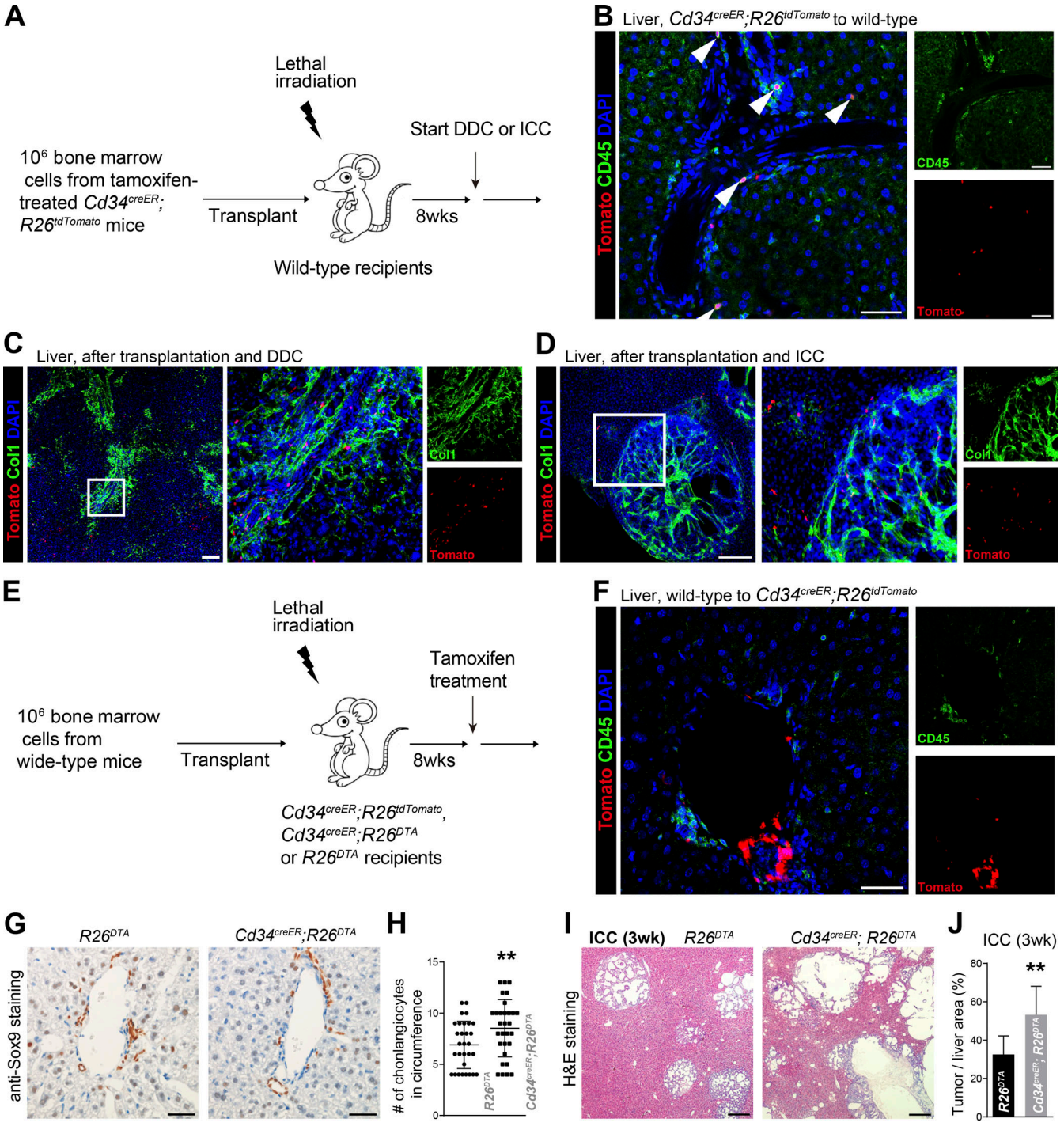

Figure 7. **CD34⁺ bone marrow cells do not contribute to liver fibrosis or ICC. (A)** Schematic of bone marrow transplantation followed by biliary fibrosis or ICC induction. **(B)** Confocal image showing Tomato expression in a subset of CD45⁺ immune cells in the liver from wild-type mice that had been transplanted with bone marrow cells from *Cd34*^{creER};*R26*^{tdTomato} mice. Arrowheads depict the Tomato⁺CD45⁺ cells. Scale bar = 50 µm (*n* = 5 mice from three independent experiments). **(C and D)** Confocal images showing no contribution of Tomato⁺ cells to Col1⁺ cells in the liver from DDC-treated (C) or ICC-bearing (D) wild-type recipients that had been transplanted with bone marrow cells from *Cd34*^{creER};*R26*^{tdTomato} mice. Scale bar = 200 µm (*n* = 5 mice from three independent experiments). **(E)** Schematic of transplantation of wild-type bone marrow cells into *Cd34*^{creER};*R26*^{tdTomato}, *Cd34*^{creER};*R26*^{DTA}, and *R26*^{DTA} recipient mice. **(F)** Confocal image showing no Tomato expression in CD45⁺ immune cells in the liver from *Cd34*^{creER};*R26*^{tdTomato} recipients. Scale bar = 50 µm (*n* = 5 mice from three independent experiments). **(G and H)** Anti-Sox9 staining of paraffin liver sections (G) from *R26*^{DTA} and *Cd34*^{creER};*R26*^{DTA} recipients. The numbers of Sox9⁺ cholangiocytes forming the circumference of the bile ducts were quantified (H). Scale bar = 100 µm (*n* = 5 mice per genotype from three independent experiments). **(I and J)** H&E staining of paraffin liver sections (I) from ICC-bearing *R26*^{DTA} and *Cd34*^{creER};*R26*^{DTA} recipients. The percentage of tumor area within liver sections was quantified (J). Scale bar = 200 µm (*n* = 5 mice per genotype from three independent experiments).

Sigma-Aldrich) for 2 days, 5% ammonium for 1 day, a tert-Butanol (360538; Sigma-Aldrich) dilution series of 30%, 50%, and 70% solutions for 4, 6 h, and 1 day, respectively, tert-Butanol/PEG (409529; Sigma-Aldrich) for 2 days, and benzyl benzoate (B6630; Sigma-Aldrich)/PEG for 1 day. 3D imaging data were acquired using a light-sheet microscope Luxendo MuVi SPIM and analyzed using Imaris software.

Bone marrow transplantation

Mice of the indicated genotype were irradiated using an RS 2000 x-ray irradiator with two doses of 540 rad (total 1,080 rad) delivered at least 2 h apart. One million whole bone marrow cells from donor mice were then injected intravenously into the retro-orbital venous sinus of irradiated recipient mice.

Quantitative real-time PCR

Cells were sorted directly into TRIzol (Life Technologies). RNA was reverse-transcribed using SuperScript III Reverse Transcriptase (Life Technologies). Quantitative real-time PCR was performed using SYBR Green on a LightCycler 96 system (Roche). Primer sequences were as follows: β-actin: 5′CGTCGACAACGGCTCCGGCATG-3′ and 5′-GGGCCTCGTCACCCACATAGGAG-3′; *Col1a1*: 5′-CACCCTCAAGAGCCTGAGTC-3′ and 5′- GTTCGGGCTGATGTACCAGT-3′; *Cd34*: 5′-TGGTAGGAACTGATGGGGAT-3′ and 5′-TGGGTAGCTCTCTGCCTGAT-3′; *Reln*: 5′-GAAACCGAGAAGCAAAGCTG-3′ and 5′-CAGGTGATGCCATTGTTGAC-3′; *Acta2*: 5′-CGAAACCACCTATAACAGCATCA-3′ and 5′-GCGTTCTGGAGGGGCAAT-3′; *Myh11*: 5′-ATCGCCCAGAAAAACAATGCCCTAAA-3′ and 5′-GCGTATCCTCCAGCTCCGTCTTGA-3′.

Analysis of single-cell transcriptomes

scRNA-seq datasets from Wang et al. (2021) and Dobie et al. (2019) were integrated, and the canonical correlation analysis method implemented in Seurat (version 4.0.1) was used to remove batch effects among different datasets. The top principal components were selected and employed for subsequent dimension reduction and unsupervised clustering. For dimension reduction, we performed t-SNE to visualize the datasets. We used the FindAllMarkers function to detect differentially expressed genes in different clusters.

Statistical methods

All data represent multiple independent experiments performed using different mice. Both male and female mice were included. Sample sizes were not based on power calculations. No randomization or blinding was performed. Variation is always indicated using standard deviation (SD). The statistical significance of differences was assessed by two-tailed Student's *t* tests.

Online supplemental material

Fig. S1, related to Fig. 1, shows the scRNA-seq analysis of non-parenchymal liver cells. Fig. S2, related to Fig. 2, shows the expression pattern of *Cd34*-CreER in the liver. Fig. S3, related to Fig. 3, demonstrates successful induction of liver fibrosis and ICC. Fig. S4, related to Fig. 4 and Fig. 5, shows the expression patterns of *Dpt*-CreER and *Acta2*-CreER in the liver. Fig. S5 shows the quantitative real-time PCR analysis of purified Tomato$^+$ cells from multiple lineage-tracing mice.

Data availability

Data supporting the findings of this study are available from the corresponding authors upon reasonable request.

Acknowledgments

This work was supported by the National Key Program on Stem Cell and Translational Research (2022YFA1104100), the Strategic Priority Research Program of Chinese Academy of Science (XDB0990000), the National Natural Science Foundation of China (32425020, 82273292, 92368101, and 32270785), Shanghai Municipal Science and Technology Major Project Fund, Shanghai Science and Technology Commission (22XD1424000 and 22ZR1469000), and Haihe Laboratory of Cell Ecosystem Innovation Fund (22HHXBSS00016).

Author contributions: S.-S. Wang: conceptualization, data curation, formal analysis, funding acquisition, investigation, methodology, project administration, supervision, validation, visualization, and writing—original draft, review, and editing. J. Yuan: data curation, formal analysis, investigation, validation, and writing—original draft. X.T. Thang: data curation and formal analysis. X. Yin: formal analysis and validation. K. Fang: data curation and investigation. L.V. Chen: formal analysis and investigation. Z. Ren: conceptualization, project administration, supervision, and writing—review and editing. B.O. Zhou: conceptualization, funding acquisition, supervision, and writing—original draft, review, and editing.

Disclosures: The authors declare no competing interests exist.

Submitted: 17 November 2023
Revised: 20 September 2024
Accepted: 8 January 2025

References

Affo, S., A. Nair, F. Brundu, A. Ravichandra, S. Bhattacharjee, M. Matsuda, L. Chin, A. Filliol, W. Wen, X. Song, et al. 2021. Promotion of cholangiocarcinoma growth by diverse cancer-associated fibroblast subpopulations. *Cancer Cell*. 39:883. https://doi.org/10.1016/j.ccell.2021.05.010

Balog, S., Y. Li, T. Ogawa, T. Miki, T. Saito, S.W. French, and K. Asahina. 2020. Development of capsular fibrosis beneath the liver surface in humans and mice. *Hepatology*. 71:291–305. https://doi.org/10.1002/hep.30809

Bhunchet, E., and K. Wake. 1992. Role of mesenchymal cell populations in porcine serum-induced rat liver fibrosis. *Hepatology*. 16:1452–1473. https://doi.org/10.1002/hep.1840160623

Brivio, S., M. Cadamuro, M. Strazzabosco, and L. Fabris. 2017. Tumor reactive stroma in cholangiocarcinoma: The fuel behind cancer aggressiveness. *World J. Hepatol.* 9:455–468. https://doi.org/10.4254/wjh.v9.i9.455

Carruthers, J.S., S.R. Kalifat, and J.W. Steiner. 1962. The ductular cell reaction of rat liver in extrahepatic cholestasis. II. The proliferation of connective tissue. *Exp. Mol. Pathol.* 1:377–396. https://doi.org/10.1016/0014-4800(62)90032-1

Chapman, G.B., and D.A. Eagles. 2007. Ultrastructural features of Glisson's capsule and the overlying mesothelium in rat, monkey and pike liver. *Tissue Cell*. 39:343–351. https://doi.org/10.1016/j.tice.2007.06.005

Chytil, A., M.A. Magnuson, C.V. Wright, and H.L. Moses. 2002. Conditional inactivation of the TGF-beta type II receptor using Cre:Lox. *Genesis*. 32: 73–75. https://doi.org/10.1002/gene.10046

Cordero-Espinoza, L., A.M. Dowbaj, T.N. Kohler, B. Strauss, O. Sarlidou, G. Belenguer, C. Pacini, N.P. Martins, R. Dobie, J.R. Wilson-Kanamori, et al. 2021. Dynamic cell contacts between periportal mesenchyme and ductal epithelium act as a rheostat for liver cell proliferation. *Cell Stem Cell*. 28: 1907–1921.e8. https://doi.org/10.1016/j.stem.2021.07.002

Dobie, R., J.R. Wilson-Kanamori, B.E.P. Henderson, J.R. Smith, K.P. Matchett, J.R. Portman, K. Wallenborg, S. Picelli, A. Zagorska, S.V. Pendem, et al. 2019. Single-cell transcriptomics uncovers zonation of function in the mesenchyme during liver fibrosis. *Cell Rep.* 29:1832–1847.e8. https://doi.org/10.1016/j.celrep.2019.10.024

Dranoff, J.A., E.A. Kruglov, S.C. Robson, N. Braun, H. Zimmermann, and J. Sévigny. 2002. The ecto-nucleoside triphosphate diphosphohydrolase NTPDase2/CD39L1 is expressed in a novel functional compartment within the liver. *Hepatology*. 36:1135–1144. https://doi.org/10.1053/jhep.2002.36823

Dranoff, J.A., and R.G. Wells. 2010. Portal fibroblasts: Underappreciated mediators of biliary fibrosis. *Hepatology*. 51:1438–1444. https://doi.org/10.1002/hep.23405

Fan, B., Y. Malato, D.F. Calvisi, S. Naqvi, N. Razumilava, S. Ribback, G.J. Gores, F. Dombrowski, M. Evert, X. Chen, and H. Willenbring. 2012. Cholangiocarcinomas can originate from hepatocytes in mice. *J. Clin. Invest.* 122:2911–2915. https://doi.org/10.1172/JCI63212

Fausther, M., J.R. Goree, E.G. Lavoie, A.L. Graham, J. Sévigny, and J.A. Dranoff. 2015. Establishment and characterization of rat portal myofibroblast cell lines. *PLoS One*. 10:e0121161. https://doi.org/10.1371/journal.pone.0121161

Filliol, A., Y. Saito, A. Nair, D.H. Dapito, L.X. Yu, A. Ravichandra, S. Bhattacharjee, S. Affo, N. Fujiwara, H. Su, et al. 2022. Opposing roles of hepatic stellate cell subpopulations in hepatocarcinogenesis. *Nature*. 610: 356–365. https://doi.org/10.1038/s41586-022-05289-6

Henderson, N.C., T.D. Arnold, Y. Katamura, M.M. Giacomini, J.D. Rodriguez, J.H. McCarty, A. Pellicoro, E. Raschperger, C. Betsholtz, P.G. Ruminski, et al. 2013. Targeting of αv integrin identifies a core molecular pathway that regulates fibrosis in several organs. *Nat. Med.* 19:1617–1624. https://doi.org/10.1038/nm.3282

Iwaisako, K., C. Jiang, M. Zhang, M. Cong, T.J. Moore-Morris, T.J. Park, X. Liu, J. Xu, P. Wang, Y.H. Paik, et al. 2014. Origin of myofibroblasts in the fibrotic liver in mice. *Proc. Natl. Acad. Sci. USA*. 111:E3297–E3305. https://doi.org/10.1073/pnas.1400062111

Jing, D., S. Zhang, W. Luo, X. Gao, Y. Men, C. Ma, X. Liu, Y. Yi, A. Bugde, B.O. Zhou, et al. 2018. Tissue clearing of both hard and soft tissue organs with the PEGASOS method. *Cell Res.* 28:803–818. https://doi.org/10.1038/s41422-018-0049-z

Karin, D., Y. Koyama, D. Brenner, and T. Kisseleva. 2016. The characteristics of activated portal fibroblasts/myofibroblasts in liver fibrosis. *Differentiation*. 92:84–92. https://doi.org/10.1016/j.diff.2016.07.001

Katsumata, L.W., A. Miyajima, and T. Itoh. 2017. Portal fibroblasts marked by the surface antigen Thy1 contribute to fibrosis in mouse models of cholestatic liver injury. *Hepatol. Commun.* 1:198–214. https://doi.org/10.1002/hep4.1023

Kisseleva, T. 2017. The origin of fibrogenic myofibroblasts in fibrotic liver. *Hepatology*. 65:1039–1043. https://doi.org/10.1002/hep.28948

Krenkel, O., J. Hundertmark, T.P. Ritz, R. Weiskirchen, and F. Tacke. 2019. Single cell RNA sequencing identifies subsets of hepatic stellate cells and myofibroblasts in liver fibrosis. *Cells*. 8:503. https://doi.org/10.3390/cells8050503

Lei, L., A. Bruneau, H. El Mourabit, J. Guegan, T. Folseraas, S. Lemoinne, T.H. Karlsen, B. Hoareau, R. Morichon, E. Gonzalez-Sanchez, C. Goumard, V. Ratziu, P. Charbord, J. Gautheron, F. Tacke, T. Jaffredo, A. Cadoret, and C. Housset. 2022. Portal fibroblasts with mesenchymal stem cell features form a reservoir of proliferative myofibroblasts in liver fibrosis. *Hepatology*. 76:1360–1375. https://doi.org/10.1002/hep.32456

Lemoinne, S., A. Cadoret, P.E. Rautou, H. El Mourabit, V. Ratziu, C. Corpechot, C. Rey, N. Bosselut, V. Barbu, D. Wendum, et al. 2015. Portal myofibroblasts promote vascular remodeling underlying cirrhosis formation through the release of microparticles. *Hepatology*. 61:1041–1055. https://doi.org/10.1002/hep.27318

Li, Y., J. Wang, and K. Asahina. 2013. Mesothelial cells give rise to hepatic stellate cells and myofibroblasts via mesothelial-mesenchymal transition in liver injury. *Proc. Natl. Acad. Sci. USA*. 110:2324–2329. https://doi.org/10.1073/pnas.1214136110

Li, Z., J.A. Dranoff, E.P. Chan, M. Uemura, J. Sévigny, and R.G. Wells. 2007. Transforming growth factor-beta and substrate stiffness regulate portal fibroblast activation in culture. *Hepatology*. 46:1246–1256. https://doi.org/10.1002/hep.21792

Lua, I., Y. Li, J.A. Zagory, K.S. Wang, S.W. French, J. Sévigny, and K. Asahina. 2016. Characterization of hepatic stellate cells, portal fibroblasts, and mesothelial cells in normal and fibrotic livers. *J. Hepatol.* 64:1137–1146. https://doi.org/10.1016/j.jhep.2016.01.010

Madisen, L., T.A. Zwingman, S.M. Sunkin, S.W. Oh, H.A. Zariwala, H. Gu, L.L. Ng, R.D. Palmiter, M.J. Hawrylycz, A.R. Jones, et al. 2010. A robust and high-throughput Cre reporting and characterization system for the whole mouse brain. *Nat. Neurosci.* 13:133–140. https://doi.org/10.1038/nn.2467

Mederacke, I., D.H. Dapito, S. Affò, H. Uchinami, and R.F. Schwabe. 2015. High-yield and high-purity isolation of hepatic stellate cells from normal and fibrotic mouse livers. *Nat. Protoc.* 10:305–315. https://doi.org/10.1038/nprot.2015.017

Mederacke, I., C.C. Hsu, J.S. Troeger, P. Huebener, X. Mu, D.H. Dapito, J.P. Pradere, and R.F. Schwabe. 2013. Fate tracing reveals hepatic stellate cells as dominant contributors to liver fibrosis independent of its aetiology. *Nat. Commun.* 4:2823. https://doi.org/10.1038/ncomms3823

Popper, H., and S. Uenfriend. 1970. Hepatic fibrosis. Correlation of biochemical and morphologic investigations. *Am. J. Med.* 49:707–721. https://doi.org/10.1016/S0002-9343(70)80135-8

Schaffner, F., T. Barka, and H. Popper. 1963. Hepatic mesenchymal cell reaction in liver disease. *Exp. Mol. Pathol.* 2:419–441. https://doi.org/10.1016/0014-4800(63)90020-0

Voehringer, D., H.E. Liang, and R.M. Locksley. 2008. Homeostasis and effector function of lymphopenia-induced "memory-like" T cells in constitutively T cell-depleted mice. *J. Immunol.* 180:4742–4753. https://doi.org/10.4049/jimmunol.180.7.4742

Wang, S.S., X.T. Tang, M. Lin, J. Yuan, Y.J. Peng, X. Yin, G. Shang, G. Ge, Z. Ren, and B.O. Zhou. 2021. Perivenous stellate cells are the main source of myofibroblasts and cancer-associated fibroblasts formed after chronic liver injuries. *Hepatology*. 74:1578–1594. https://doi.org/10.1002/hep.31848

Wells, R.G. 2014. The portal fibroblast: Not just a poor man's stellate cell. *Gastroenterology*. 147:41–47. https://doi.org/10.1053/j.gastro.2014.05.001

Wendling, O., J.M. Bornert, P. Chambon, and D. Metzger. 2009. Efficient temporally-controlled targeted mutagenesis in smooth muscle cells of the adult mouse. *Genesis*. 47:14–18. https://doi.org/10.1002/dvg.20448

Yang, W., H. He, T. Wang, N. Su, F. Zhang, K. Jiang, J. Zhu, C. Zhang, K. Niu, L. Wang, et al. 2021. Single-cell transcriptomic analysis reveals a hepatic stellate cell-activation roadmap and myofibroblast origin during liver fibrosis in mice. *Hepatology*. 74:2774–2790. https://doi.org/10.1002/hep.31987

Supplemental material

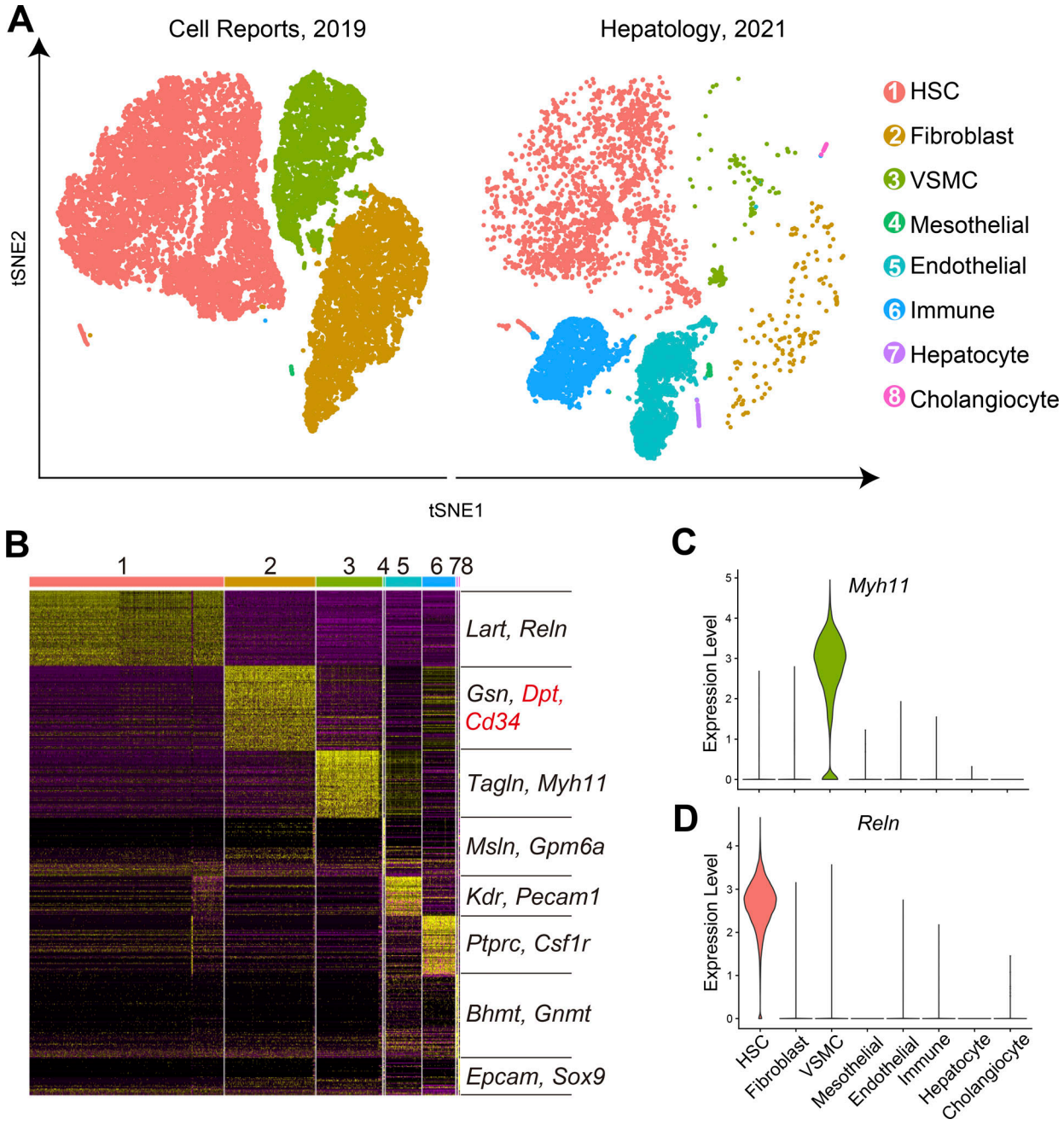

Figure S1. **scRNA-seq analysis of non-parenchymal liver cells. (A)** Visualization of unsupervised clustering in a t-SNE plot of liver cells from Dobie et al. (2019) and Wang et al. (2021). **(B)** Heatmap showing the top 100 differentially expressed genes in each cell cluster. **(C and D)** Violin plots showing the expression levels of *Myh11* (C) and *Reln* (D) in different cell clusters.

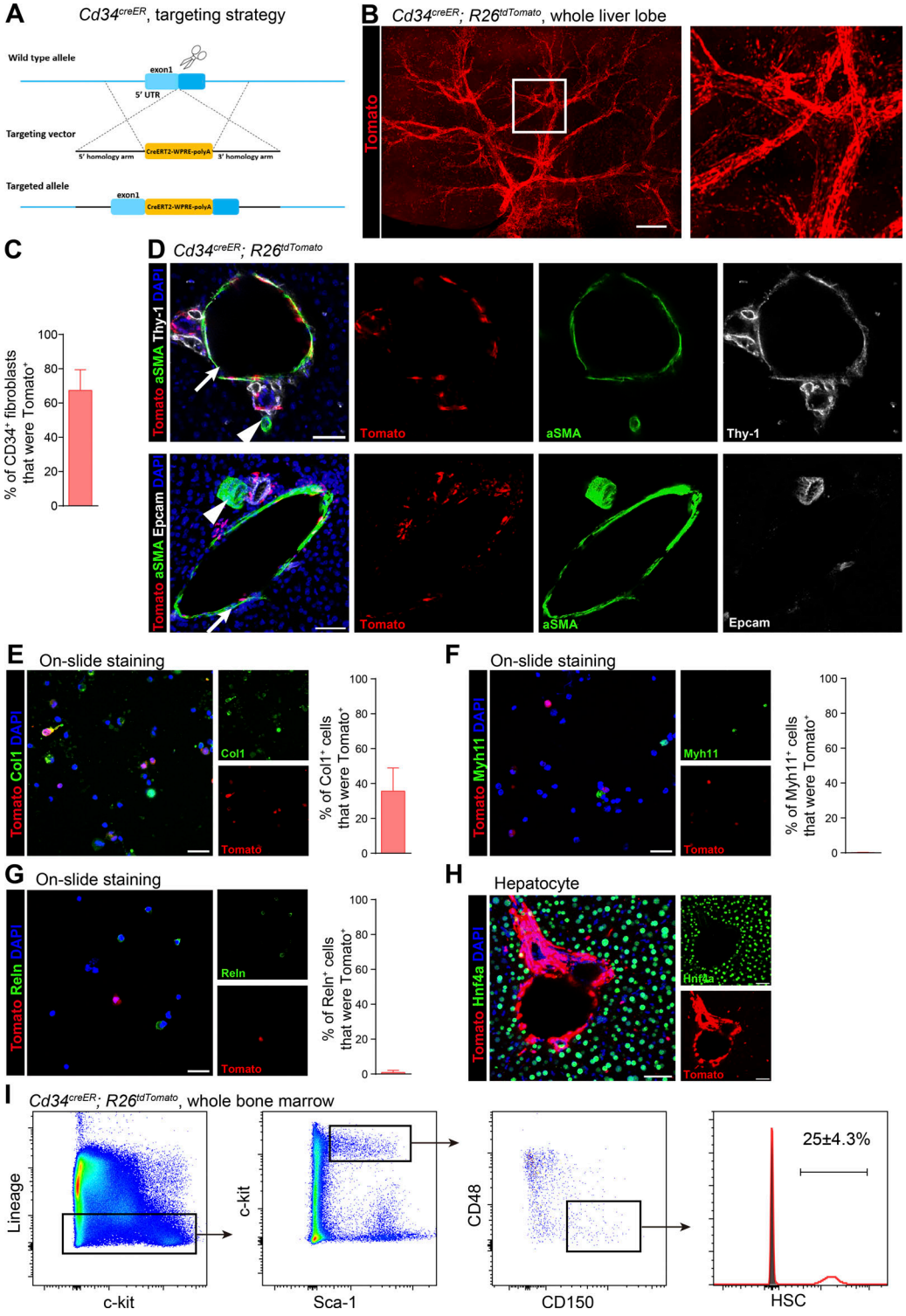

Figure S2. **Characterization of *Cd34*^{creER};*R26*^{tdTomato} mice. (A)** Schematic of the design of *Cd34*^{creER} mice. **(B)** Three-dimensional reconstruction of whole liver from *Cd34*^{creER};*R26*^{tdTomato} mice. Samples were cleared using the PEGASOS method, and images were captured using a light-sheet microscope. Scale bar = 500 µm. **(C)** Quantification of the percentage of CD34$^+$ fibroblasts that were Tomato$^+$ on the liver sections from *Cd34*^{creER};*R26*^{tdTomato} mice. **(D)** Confocal image showing Tomato expression in the portal space of *Cd34*^{creER};*R26*^{tdTomato} mice. Anti-Thy-1 staining identified portal fibroblasts surrounding portal veins and bile ducts, while anti-aSma staining labeled VSMCs surrounding arteries and portal veins (upper). Bile ducts and arteries were distinguished by anti-Epcam and anti-aSma antibodies (bottom). Arrows depict the portal vein; arrowheads depict the hepatic artery. Scale bar = 50 µm. **(E–G)** On-slide staining of non-parenchymal liver cells from *Cd34*^{creER};*R26*^{tdTomato} mice with anti-Col1 (E), anti-Myh11 (F), and anti-Reln (G) antibodies, respectively. Cells were isolated by gradient centrifugation and were mounted on poly-D-lysine–coated slides. Scale bar = 25 µm. **(H)** Confocal image showing no Tomato expression in Hnf4a$^+$ hepatocytes in *Cd34*^{creER};*R26*^{tdTomato} mice. Scale bar = 50 µm. **(I)** Flow cytometric analysis of cells from whole bone marrow showing that ∼25% of all hematopoietic stem cells were Tomato$^+$ in *Cd34*^{creER};*R26*^{tdTomato} mice.

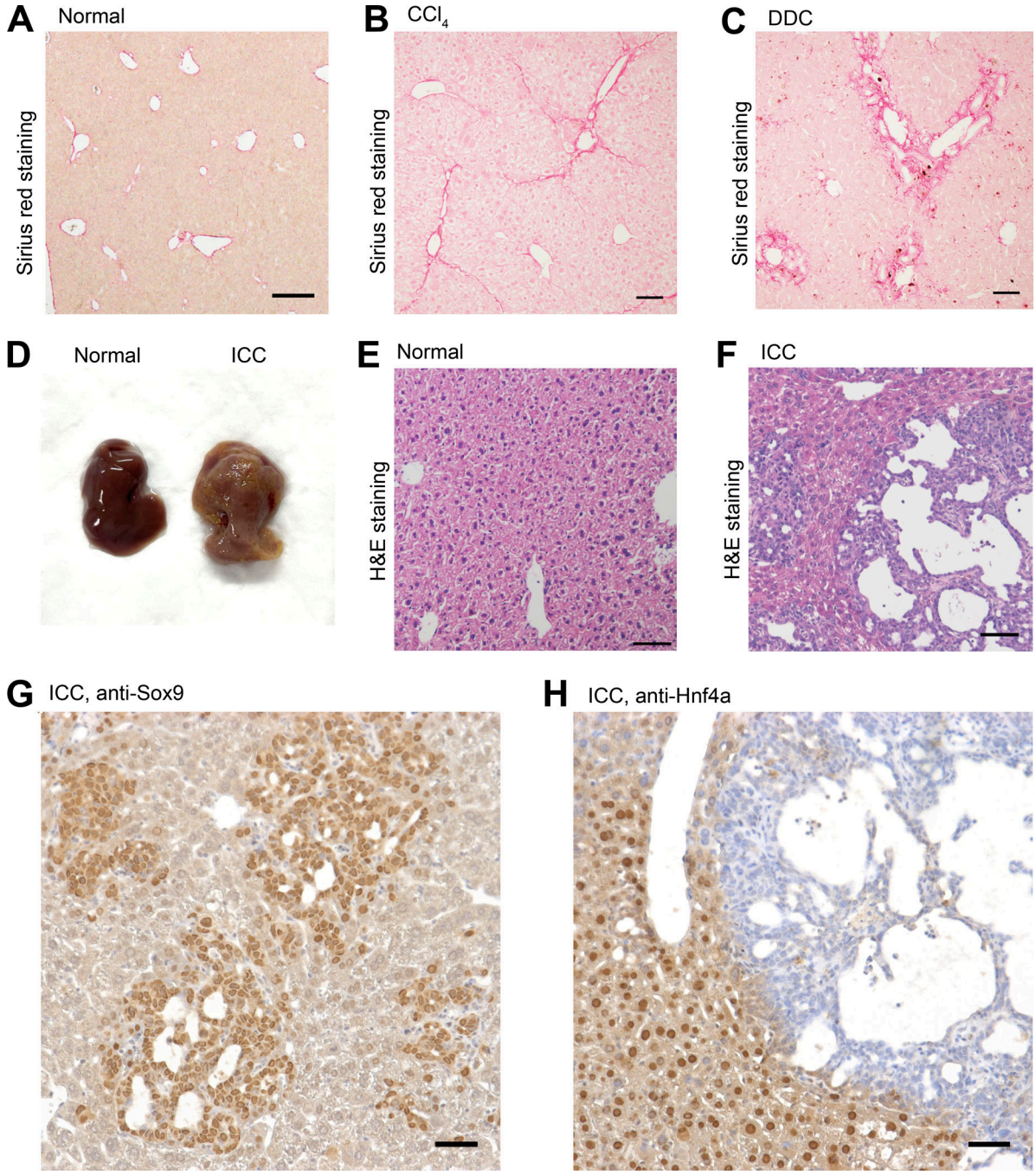

Figure S3. **Successful induction of liver fibrosis and ICC. (A–C)** Sirius red staining of paraffin liver sections from normal (A), CCl_4-treated (B), and DDC-treated (C) *Cd34*^{creER};*R26*^{tdTomato} mice. Scale bar = 200 µm (n = 5 mice from three independent experiments). **(D)** Photographs of normal and ICC-bearing livers (n = 5 mice from three independent experiments). **(E and F)** H&E staining of normal (E) and ICC-bearing (F) *Cd34*^{creER};*R26*^{tdTomato} mice. Scale bar = 200 µm (n = 5 mice from three independent experiments). **(G and H)** Anti-Sox9 (G) and anti-Hnf4a (H) staining of paraffin sections of ICC-bearing livers. Scale bar = 100 µm (n = 5 mice from three independent experiments).

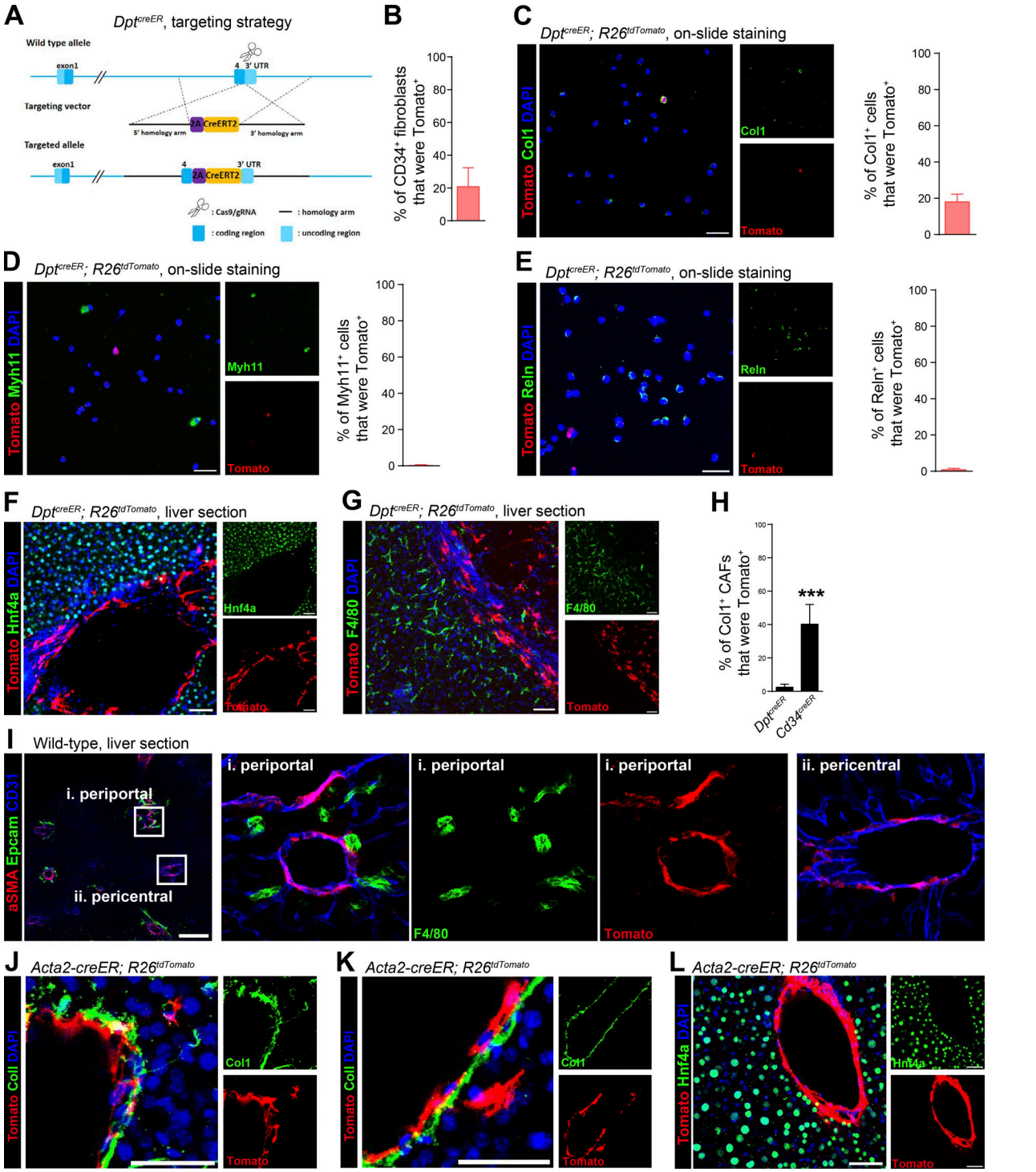

Figure S4. **Characterization of *Dpt*^{creER};*R26*^{tdTomato} and *Acta2-creER;R26*^{tdTomato} mice. (A)** Schematic of the design of *Dpt*^{creER};*R26*^{tdTomato} lineage-tracing mice. **(B)** Quantification of the percentage of CD34$^+$ fibroblasts that were Tomato$^+$ on the liver sections from *Dpt*^{creER};*R26*^{tdTomato} mice. **(C–E)** On-slide staining of non-parenchymal liver cells from *Dpt*^{creER};*R26*^{tdTomato} mice with anti-Col1 (C), anti-Myh11 (D), and anti-Reln (E) antibodies, respectively. Cells were isolated by gradient centrifugation and were mounted on poly-D-lysine–coated slides. Scale bar = 25 µm. **(F and G)** Confocal images showing that Tomato was not expressed in Hnf4a$^+$ hepatocytes (F) or F4/80$^+$ Kupffer cells (G) in the livers from *Dpt*^{creER};*R26*^{tdTomato} mice. Scale bar = 50 µm (n = 5 mice from three independent experiments). **(H)** Statistical analysis of the percentage of CAFs derived from *Cd34*-CreER$^+$ and *Dpt*-CreER$^+$ cells in ICCs. The statistical significance of differences was assessed by two-tailed Student's t tests. ***P < 0.001. **(I)** Confocal images of liver sections (15 µm) showing the protein expression patterns of aSma. Blood vessels and bile ducts were labeled by anti-CD31 and anti-Epcam antibodies, respectively. Scale bar = 200 µm (n = 3 mice from three independent experiments). **(J and K)** High-magnification confocal images showing the distributions of Tomato$^+$ cells and Col1$^+$ cells in the livers from *Acta2;R26*^{tdTomato} mice. J represents a magnified view of Fig. 5 E. Scale bar = 50 µm (n = 3 mice from three independent experiments). **(L)** Confocal images showing that Tomato was not expressed in Hnf4a$^+$ hepatocytes in the liver from *Acta2;R26*^{tdTomato} mice. Scale bar = 50 µm (n = 3 mice from three independent experiments).

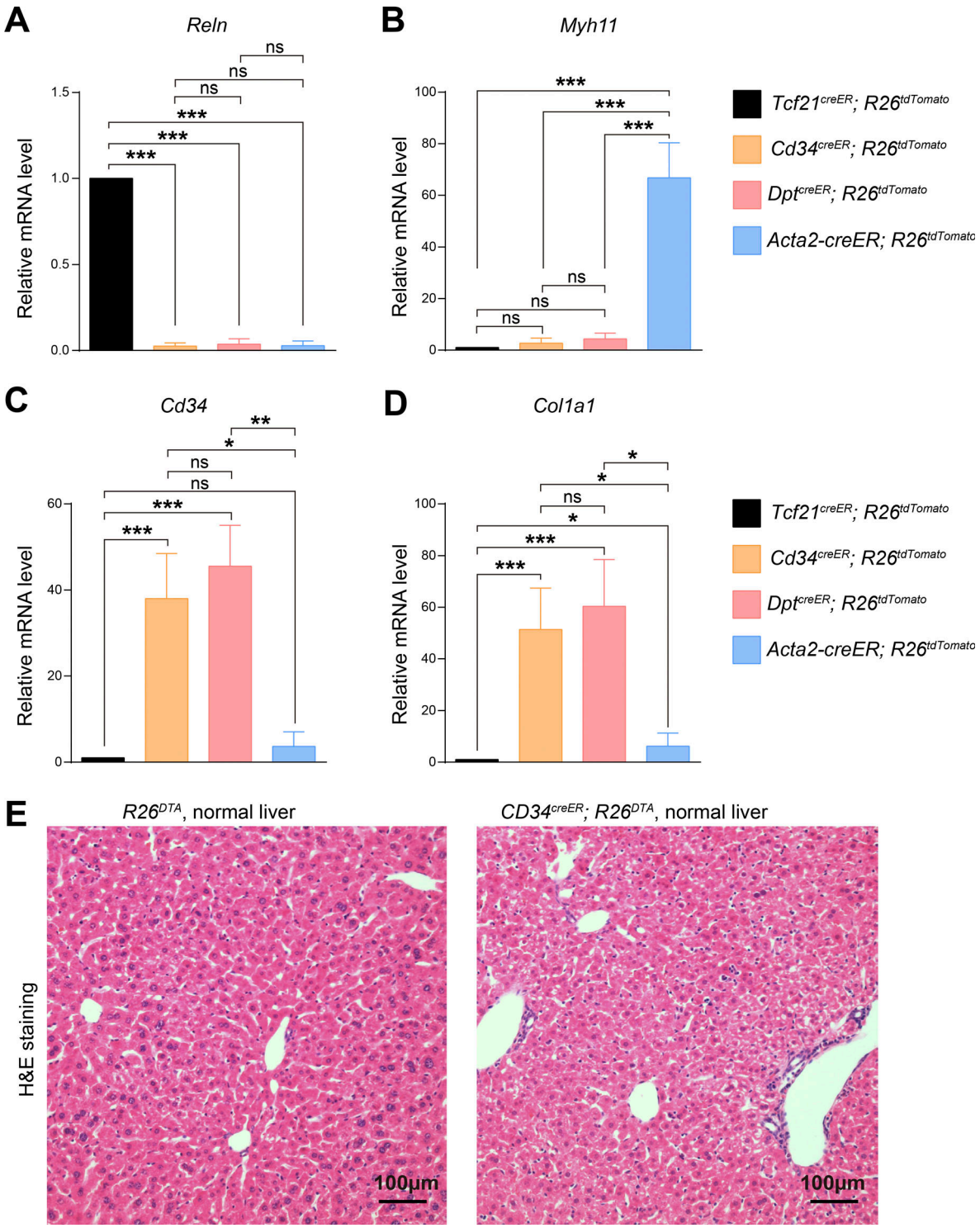

Figure S5. **Quantitative real-time PCR analysis of purified Tomato⁺ cells. (A–D)** Real-time PCR analysis of mRNA levels of *Reln* (A), *Myh11* (B), *Cd34* (C), and *Col1a1* (D) in purified Tomato⁺CD45⁻ liver cells from mice of the indicated genotype. The statistical significance of differences was assessed by two-tailed Student's *t* tests. *P < 0.05, **P < 0.01, ***P < 0.001 (*n* = 5 mice per genotype from three independent experiments). **(E)** H&E staining of liver sections from *Cd34*^{creER};*R26*^{DTA} and *R26*^{DTA} mice at 2 wk after tamoxifen treatment. Scale bar = 100 μm.